



Minnesota State University, Mankato  
Cornerstone: A Collection of Scholarly  
and Creative Works for Minnesota  
State University, Mankato

---

All Graduate Theses, Dissertations, and Other  
Capstone Projects

Graduate Theses, Dissertations, and Other  
Capstone Projects

---

2018

## Comparative Study of CV3 Carbonaceous Chondrites Allende and Bali Using Micro-Raman Spectroscopy and SEM/EDS

Raka Paul  
*Minnesota State University, Mankato*

Follow this and additional works at: <https://cornerstone.lib.mnsu.edu/etds>

 Part of the [Astrophysics and Astronomy Commons](#), [Materials Science and Engineering Commons](#),  
and the [Physics Commons](#)

---

### Recommended Citation

Paul, R. (2018). Comparative Study of CV3 Carbonaceous Chondrites Allende and Bali Using Micro-Raman Spectroscopy and SEM/EDS [Master's thesis, Minnesota State University, Mankato]. Cornerstone: A Collection of Scholarly and Creative Works for Minnesota State University, Mankato. <https://cornerstone.lib.mnsu.edu/etds/837/>

This Thesis is brought to you for free and open access by the Graduate Theses, Dissertations, and Other Capstone Projects at Cornerstone: A Collection of Scholarly and Creative Works for Minnesota State University, Mankato. It has been accepted for inclusion in All Graduate Theses, Dissertations, and Other Capstone Projects by an authorized administrator of Cornerstone: A Collection of Scholarly and Creative Works for Minnesota State University, Mankato.

Comparative study of CV3 carbonaceous chondrites Allende and Bali using micro-Raman spectroscopy and SEM/EDS

By

Raka Paul

A Thesis Submitted in Partial Fulfillment of the

Requirements for the Degree of

Master of Science

In

Physics

Minnesota State University, Mankato

Mankato, Minnesota

November 2018

11/16/2018

Comparative study of CV3 carbonaceous chondrites Allende and Bali using micro-Raman spectroscopy and SEM/EDS.

Raka Paul

This thesis has been examined and approved by the following members of the student's committee.

---

Dr. Analía Dall'Asén, Advisor

---

Dr. Andrew Roberts, Committee Member

---

Dr. Steven Losh, Committee Member

Comparative study of CV3 carbonaceous chondrites Allende and Bali using micro-Raman spectroscopy and SEM/EDS.

Raka Paul

M.S., Physics

Minnesota State University, Mankato

2018

## Abstract

The birth of the solar system (over 4 billion years) is speculated to have happened from a nebula, swirling and compacting in localized regions to eventually form the Sun and planets. This complex process consists of numerous changes and intermediary steps, yet to be fully understood. Carbonaceous chondritic meteorites are relics of that process and therefore have potential to reveal information about the formation history. Several theories have been formulated linking their composition to planet formation. This study focusses on two carbonaceous chondritic specimens, Allende and Bali, both of the group CV and petrologic type 3. CV meteorites are abundant in inclusions (e.g. chondrules), which are considered the oldest objects to have formed in the solar system. Samples were studied using micro-Raman spectroscopy, scanning electron microscopy and energy dispersive X-ray spectroscopy (SEM/EDS). Chondrules were identified in the Allende sample, while Bali had several irregular inclusions and small crystals. These other inclusions were refractory inclusions rich in Ca and Al. Elements common to both were: O, Si, Fe, Mg, C and S. Ni, Ca and Al were also present but varied in relative percentage weight in each sample. Bali had several Fe-Ni spots, while no such spots were identified in Allende. S-rims were seen around inclusions in both, as was the Fe/Mg complementarity between matrix and inclusion. Minerals found in both were graphitic carbon and Mg-rich olivine. Allende also contained pyroxene and quartz; while Bali had larnite, magnetite and awaruite. Information obtained about the parent bodies of these samples includes their peak metamorphic temperatures and extent of secondary alterations (post-accretion). Allende was found to be more metamorphosed than Bali. Possible implications from the obtained results have been discussed in the light of planet formation models, such as that the formation of the inclusions and surrounding matrix

could have taken place in the same local nebular region. Overall, the findings from this study agree well with literature and add to the studies conducted within the planet formation community.

# Table of Contents

## 1. Introduction1

1.1 An Overview .....	1
1.2 Meteorites.....	3
1.2.1 Classification Scheme.....	4
1.2.2 Carbonaceous chondrites.....	7
1.3 Raman spectroscopy	
1.3.1 Principle.....	9
1.3.2 Instrumentation.....	12
1.3.3 Applications.....	13
1.4 Scanning Electron Microscopy	
1.4.1 Principle .....	14
1.4.2 Instrumentation .....	16
1.4.3 Applications .....	17
1.5 Energy Dispersive X-ray Spectroscopy (EDS)	
1.5.1 Principle .....	18
1.5.2 Instrumentation and applications.....	20

## 2. Experimental Methods

2.1 Samples .....	22
2.1.1 Allende .....	22
2.1.2 Bali.....	24
2.1.3 Examined regions.....	25
2.2 Raman spectroscopy	
2.2.1 Experimental Setup and Procedure .....	26
2.2.2 Data Acquisition and Analysis .....	29
2.2.3 Mineral Identification .....	32
2.3 SEM/EDS	
2.3.1 Experimental Setup and Procedure .....	32

2.3.2 Data Acquisition and Analysis .....	35
<b>3. Results and Data Analysis</b>	
3.1 Allende	
3.1.1 Raman spectroscopy .....	36
3.1.2 SEM/EDS .....	41
3.2 Bali	
3.2.1 Raman spectroscopy .....	49
3.2.2 SEM/EDS .....	53
<b>4. Discussion</b>	
4.1 Features and trends within each chondritic sample .....	59
4.2 Features and trends between the two chondritic samples .....	63
4.3 Justifications toward a single local parent reservoir .....	68
4.4 Carbon peak parameters and secondary alterations of the parent body .....	70
<b>5. Conclusion</b> .....	76
<b>6. Acknowledgements</b> .....	79
<b>7. References</b> .....	81

# 1. Introduction

## 1.1 An Overview

Unraveling the birth and evolution of the solar system has attracted and continues to attract researchers, since a long time. Despite much progress in this field a clear picture detailing every step of the process is yet to be achieved. State-of-the-art telescopes capable of distant astronomical observations and spacecraft missions to collect extra-terrestrial samples have been two primary methods of studying the outer space, including the solar system. However, the exorbitant cost factors and number of constraints involved are major limitations in frequent implementation of these methods. A third option which is much cost effective and is an equally reliable source of information is the study of meteorites. Eliminating the hassle of sample acquisition from its native source while ensuring the quality of the samples, meteorite studies reveal a wide variety of data about the formation history of the solar system. Over the years, meteorites have been classified based on their structure and chemistry. One of the meteoritic subtypes: chondrites or chondrule bearing meteorites particularly hold significant importance in understanding the solar system evolution (Sears, 2004). They happen to be the largest group of meteorites and have been widely studied. With newer and advanced techniques available to scientists, the chondrites continue to provide unique insights about their origin.

Modern theories describe the process of planet formation, starting with a swirling protoplanetary disk, building planetesimals from the dust within it, and growing

protoplanets (parent bodies) out of a storm of collisions. In the solar system, a chronology of planet formation emerges from radiometric measurements of meteorites. Chondritic meteorites, objects that formed early and remained relatively pristine since the time of their formation, contain important clues as to how planets form (Dall'Asén et al, 2017). Chondrites are a kind of cosmic sediment, composed of diverse materials with mostly nebular origins. They are the residual cosmic matter that had never collected into planets but that had formed when conditions at the Sun's surface extended farther out into the solar system (McSween 1999).

A major debate surrounding the chondrite formation (and hence planetary formation) lies between the ideas that whether the chondrule and matrix formation took place in the same local nebular region (Palme et al., 2015, Hezel and Palme, 2008, 2010 etc.) or whether they were instead formed at separate zones in the nebula (accretionary disk) and later coagulated into chondrites (Shu et al., 2001, Zook, 1981 etc.)..

Studying the properties of meteorites (e.g. mineral and elemental composition, structure, topography, aging, etc.) can help to answer these questions and other questions about planet formation. For this purpose, various analytical techniques are employed to analyze meteoritic samples. Chemical (wet) analysis, X-ray diffraction, radiometry, electron microscopy and Raman spectroscopy are some of the commonly used techniques.

In this study, Raman spectroscopy and scanning electron microscopy (SEM) along with energy-dispersive X-ray spectroscopy (EDS) have been applied to analyze

two meteoritic samples. The major advantage of the aforementioned methods is that they are non-destructive and require no sample preparation. Thus the sample can be preserved for future studies. Raman spectroscopy gives information about the minerals from their chemical bonds present in the sample, with each mineral being identified from its signature spectra. SEM imaging provides morphological and textural details about the sample surface, while EDS gives information about its elemental composition.

In this work, justifications for multiple findings, obtained using the aforementioned techniques to analyze the Allende and Bali meteoritic samples, are presented and explained in detail showing that they can together support the hypothesis of a single (local) parent reservoir for the chondrules and matrix. In addition, analyses have been done to obtain and quantify some of the alterations experienced by the post-accretion parent bodies of the meteorites. Furthermore, to the best of this research group's knowledge, only a few works have reported findings about the Bali meteoritic sample (Stoffler 1991, Keller *et al.*, 1994) thus this study adds to the research that has been conducted on carbonaceous chondritic meteorites

## **1.2 Meteorites**

In its orbit around the Sun, the Earth frequently encounters solid objects called meteoroids. When a meteoroid enters the Earth's atmosphere, friction in the air causes heating of the outer layer. Depending on the extent of heating, fusion may occur and the outer layer of dust and material around the incoming object becomes incandescent. It

appears as a streak of light falling from the sky, and is called meteors (Hutchinson, 2004). Depending on the meteor size, fragments of it reaches the ground even after most of it gets burned away. Some of these fragments, known as meteorites, are then recovered and examined by experts. If a falling meteor was observed to reach the ground, its meteorites are categorized as ‘falls’. Unlike the fragments of those meteors which were discovered on the ground itself, and are classified as ‘finds’. Over the last couple centuries, a vast number of meteorites have been collected and analyzed systematically. It was consequently revealed that the variety of meteorites available, each type containing an abundance of information; needed a classification scheme(s) based on their differences in structure, composition etc. Meteorite classification is quite complex, since they can be categorized on the basis of several distinguishing factors. A general classification scheme which is widely accepted and covers most of the vital features is elaborated below.

### 1.2.1 Classification Scheme

Figure 1.2.1 shows a schematic of the meteorite subtypes and clans. As illustrated, meteorites can be broadly classified to belong to each of the four types: Stony (94% of falls), Irons (5%) or Stony-irons (1%) (McSween, 1999). Each of these types has been further subdivided. For the purposes of this work, only the chondrites with its corresponding subtype studied here: carbonaceous, has been expanded upon.

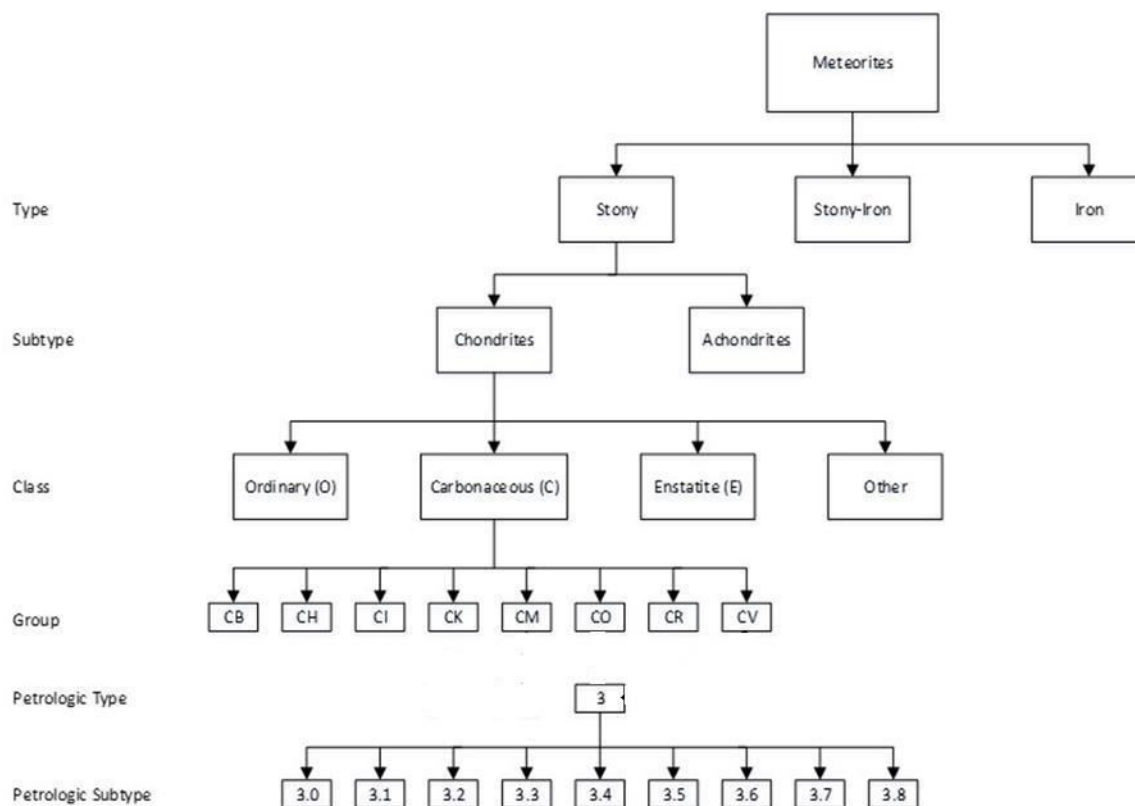


**Figure 1.1.** Classification scheme of meteorites (Stokke, 2018, adapted from Hutchinson, 2004; Weisberg et al., 2006).

The Stony meteorites are subdivided into chondrites or achondrites. Most meteorites (~86%) are chondrites, they are named after the white globules called chondrules that are embedded within a rocky substance (the matrix). In addition to chondrules and the matrix, the other materials contained in chondrites are refractory inclusions, metal deposits and sulfides (Sears, 2004).

Each of the chondritic components is briefly discussed below (McSween and Huss, 2010):

- Chondrules: These droplets were formed by flash melting at temperatures of 1770-2120 K, and subsequently experienced rapid cooling and solidification in minutes to hours. The heating mechanisms for chondrules remain a contentious subject. However, their cooling rates are fairly well constrained by laboratory experiments that reproduce the distinctive textures of chondrules. They underwent several cycles of heating and recrystallization.
  
- Refractory Inclusions: Inclusions containing elements or minerals that are 'refractory' i.e. much resistant to heat and wear, (as opposed to volatile elements) are some of the first materials that formed in the chondrites, around 4.5 billion years ago. This is because the minerals in these inclusions tend to crystallize at very high temperatures (McSween, 1999). They have been classified into two subtypes, calcium-aluminum-rich inclusions (CAIs) which are rich in Ca-Al minerals and amoeboid-olivine-aggregates (AOAs) that are irregularly shaped and have high forsterite content.
  
- Metals and sulfides: small nuggets of Fe-loving (siderophile) elements such as Os, Mo etc., along with grains of Fe-containing alloy (Fe-Ni, Fe-Ni-Co etc.) occur within and as rims on chondrules. Sulfide in the form of troilite (FeS) is also commonly found within the chondrites. Most of these refractory alloys are predicted to condense at temperatures >1600 K from a gas of solar composition.
  
- Matrix: The substance that cements all the other chondritic components together is called the matrix. It is an optically opaque (in thin section) assortment of very fine-grained minerals such as silicates, oxides. The origin of matrix materials is uncertain;

they are probably complex mixtures of presolar grains, nebular condensates, disaggregated chondrules and refractory inclusions.

### 1.2.2 Carbonaceous chondrites

When first discovered, the carbonaceous chondrites were thought to be the only class to contain carbon. Despite what their name seems to imply, these meteorites only contain <1 to ~6 wt. % carbon. The carbonaceous class is considered the most primitive of the classes as their ratio of nonvolatile (or refractory) elements (Fe, Si, Mg, Al, Ca, etc.) is very similar to that of the sun (Stokke, 2018). Carbonaceous chondrites (the class of chondrites studied in this work) is a large clan with several different groups: CB, CH, CI, CK, CM, CO, CR, and CV. The first letter “C” stands for “carbonaceous”, and the second letter indicates the location where the most prominent meteorite with similar composition originated, except for CH where “H” stands for “high metal”. For example, “I” stands for “Ivuna” (Tanzania), and “V” stands for “Vigarano” (Italy) (Weisberg et al., 2006). Except for CI chondrites, all of the carbonaceous chondrites contain chondrules (McSween and Huss, 2010).

Once this primary classification has been done, chondrites are further subdivided based on the type and extent of alterations (secondary) that they underwent in their parent bodies. This is reflected by the petrologic type (PT) which they belong to (Fig. 1.2.2).

Petrologic Type						
1	2	3	4	5	6	7
← Increasing aqueous alteration		"Pristine"	Increasing thermal metamorphism →			

**Figure 1.2.** Petrologic sequence of chondrites (Stokke, 2018; adapted from Norton and Chitwood, 2008, and McSween and Huss, 2010).

Among the Petrologic types (1 to 7), type 3 chondrites are the ones that were least altered. These chondrites underwent some thermal metamorphosis along with aqueous alterations, but relatively less as indicated by the direction of arrows. The samples studied here: Allende and Bali both belong to the CV group and PT subgroup 3. Sears et al. (1980) subdivided type 3 chondrites into types 3.0 to 3.9 (with thermal alteration increasing from lower to higher) based on their thermoluminescence (TL), which is a measure of the induced luminescence by a dose of radiation (McSween, 1999).

Furthermore, the CV3 chondrites show a diversity of secondary characteristics that have resulted in their subdivision into two subgroups, the oxidized CV3s ( $CV_{3_{ox}}$ ) and the reduced CV3s ( $CV_{3_{red}}$ ), primarily on the basis of the metal content in them (McSween, 1977). The oxidized subgroup has been subsequently divided into the Allende-like ( $CV_{oxA}$ ) and Bali-like ( $CV_{oxB}$ ) sub-groups (Krot et al, 1998), based on the differences in their compositions of inclusions and matrix, and the degree of thermal alteration. Hence, all CV3 chondrites that were oxidized in their parent bodies fall into either category. For example, Axtell and Vigarano are  $CV_{oxA}$  while Kaba and Grosnaja are  $CV_{oxB}$  (Krot et al, 1998).

## 1.3 Raman spectroscopy

### 1.3.1 Principle

When a molecule interacts with an electromagnetic (EM) field, a transfer of energy takes place from the field to the molecule if Bohr's frequency condition (equation 1) is satisfied (Ferraro et al., 2002). Suppose, the molecule was initially at its ground state with energy  $E_1$ , and after absorption of energy from the EM field, the molecule jumps to a higher energy state  $E_2$ , then:

$$\Delta E = h\nu = h\frac{c}{\lambda} = hc\nu' \quad (1)$$

Where  $\Delta E$  is the difference in energy (in erg) between the two quantized states (1 and 2),  $h$  is Planck's constant ( $6.62 \times 10^{-27}$  erg s),  $c$  is the velocity of light (in cm/s),  $\lambda$  (in cm) is the wavelength of the EM wave and  $\nu'$ , which is commonly encountered in vibrational spectroscopy is the "wavenumber" (in  $\text{cm}^{-1}$ ), defined as:

$$\nu' = \frac{\nu}{c} = \frac{1}{\lambda} \quad (2)$$

As an example, a  $\lambda = 4000 \text{ \AA}$  would correspond to  $\nu' = 2.5 \times 10^3 \text{ cm}^{-1}$ .

Depending upon the excitation energy of the incident EM wave, a molecule may undergo one or more types of transitions in its energy levels. Once, the molecule reaches a higher energy level, it emits an amount of energy (equal to the difference between the energies of the two levels,  $\Delta E$ ) before returning to the ground state.

In Raman spectroscopy, the sample is irradiated by an intense laser beam in the UV-visible region ( $\nu_0$ ), i.e.  $10 \text{ nm} < \lambda < 700 \text{ nm}$ ; the (inelastic) scattered light emitted by the molecules is usually observed in the direction perpendicular to the incident beam. The scattered light consists of two types: one is the Rayleigh scattering, which is strong and has the same frequency as the incident beam ( $\nu_0$ ), and the other is called Raman scattering which is very weak ( $\sim 10^{-5}$  times the intensity of incident beam) and has frequencies ( $\nu_0 \pm \nu_m$ ), where  $\nu_m$  is a vibrational frequency of a molecule. The ( $\nu_0 - \nu_m$ ) and ( $\nu_0 + \nu_m$ ) lines are called Stokes and anti-Stokes lines, respectively. Not all molecules can be excited to obtain Raman vibrational frequencies. If the molecule is not polarizable by the incident light, i.e. if the vibrations do not bring about a separation between its positive charge center and electron cloud, the vibration is said to be Raman-inactive (Ferraro et al., 2002).

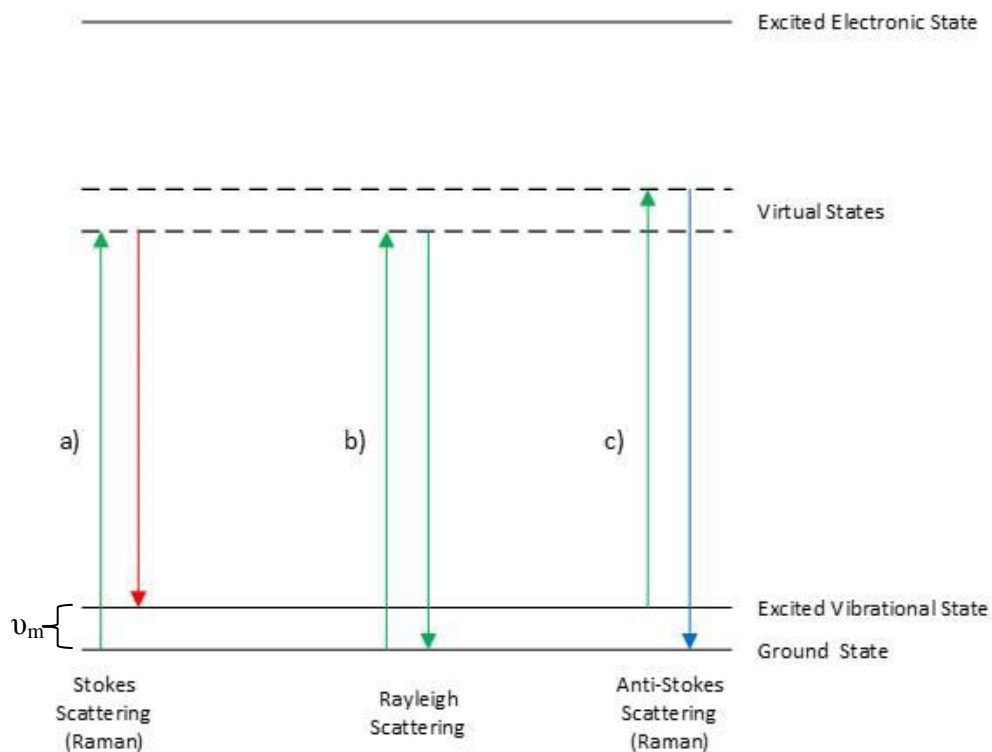


**Figure 1.3.** Energy level diagram (not to scale) illustrating vibrational energy transitions of molecules in Raman spectroscopy (Stokke, 2018): (a) Stokes scattering (Raman), (b) Rayleigh scattering, and (c) anti-Stokes scattering (Raman). The incident photon energy and the scattered photon energy are represented by the arrow pointing “up” and “down”, respectively. The difference between the molecule’s excited vibrational frequency and the incident frequency corresponds to a frequency  $\nu_m$ .

To achieve the Raman spectra from a Raman-sensitive sample, it is first excited with some incident light. This excites a molecule in the sample to some virtual energy state, below the first excited electronic state. This unobservable virtual state decays extremely quickly and therefore does not violate the energy-time uncertainty principle (Stokke, 2018). At room temperature, there is a higher probability of molecules being in the ground state than an excited state (Fig. 1.4) so Stokes lines have a greater intensity than anti-Stokes lines (Ferraro et al. 2002; Raman 1929).

In a sample comprised of various materials (minerals, alloys) inelastic scattering by each material produces characteristic shifts in the wavelength that can be measured by a spectrometer (McSween and Huss, 2010). Figure 1.4 illustrates a Raman spectrum for industrial diamond with a characteristic peak position at  $\sim 1335 \text{ cm}^{-1}$ .

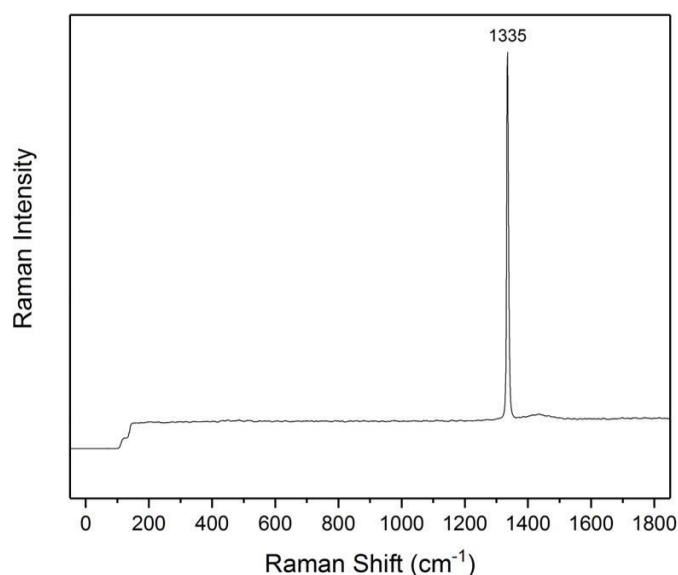


**Figure 1.4.** Raman spectrum for industrial diamond with characteristic peak position at  $\sim 1335 \text{ cm}^{-1}$  (Stokke, 2018).

### 1.3.2 Instrumentation

In 1928, Sir Chandrashekhara Venkata Raman discovered the phenomenon that bears his name. Sir Raman used sunlight as the source and a telescope as the collector; the detector was his eyes (Ferraro et al., 2002). He was awarded the 1930 Nobel prize in physics for his remarkable discovery.

Nowadays, Raman spectrometers consist of the following main components: excitation source (which is generally a continuous wave laser), sample illumination,

optical collection system, spectrograph (with optical elements to disperse the scattered light into different wavelengths), detector and computer control/processing systems.

The incident laser beam is directed using appropriate optics (e.g. fiber optics cables, lenses, mirrors, filters, etc.) to irradiate the sample with the desired power. After interacting with the sample, the scattered light is collected with optical elements (e.g. microscope objective) and sent to a spectrograph (with a prism or diffraction grating) to split the signal into its constituent wavelengths. This new signal is sent to a detector that is attached to the spectrograph (such as a photomultiplier tube or charge-couple device) and the output is displayed on a computer monitor.

### 1.3.3 Application

Being a non-invasive technique, Raman spectroscopy can be used in a wide arena of fields: science laboratories, industries, medical etc. Also, the results are obtained relatively faster than most experimental methods and therefore Raman spectroscopy is used as a commercial tool for quality control and check. In many scientific disciplines such as material sciences, physics, chemistry etc., Raman spectroscopy finds applications since it can be used to measure spectra from many different types of materials including gases, liquids, solutions, crystals, and amorphous solids. Some examples of application in both research and industry include: determining polymorphs and phase transitions of solids, detecting hazardous materials in ground water, diagnosing malignant tissues in the human body, and identifying illicit drugs (Stokke, 2018). Over past several decades, several adaptations have been made to the Raman system to accommodate a variety of

specialized measurements such as Surface-Enhanced Raman Spectroscopy (SERS), Tip-Enhanced Raman spectroscopy (TERS), and high-pressure Raman spectroscopy.

## **1.4 Scanning Electron Microscopy (SEM)**

### **1.4.1 Principle**

Similar to the process of irradiation with photons as was discussed earlier, scanning electron microscopy uses an electron beam to study the sample features. The beam electrons interact with the specimen atoms through a variety of physical processes collectively referred to as “scattering events”. The overall effects of these scattering events are to transfer energy to the specimen atoms from the beam electrons, thus setting a limit on their travel within the solid, and to alter the direction of travel of the beam electrons away from their incident trajectory. These beam electron-specimen interactions produce the Backscattered electrons (BSE), secondary electrons (SE) and X-rays that convey information about the specimen such as coarse- and fine-scale topographic features, composition, crystal structure etc. (Goldstein et al, 2018). Figure 1.5 shows a schematic of the process of incident electrons on a specimen and the ejected electrons going outward from the sample.

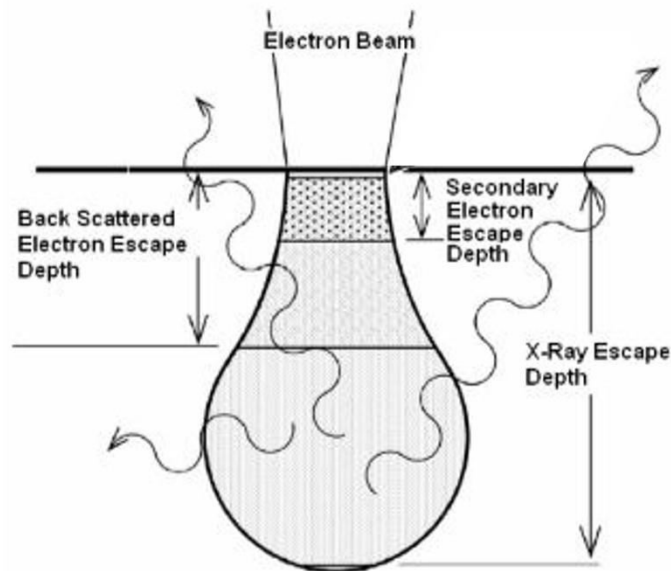


**Figure 1.5.** Diagram of the relative escape depths (not to scale) of electrons and characteristic X-rays in a sample (original image from Hafner, 2015).

A significant fraction of the incident beam electrons undergo sufficient scattering events to completely reverse their initial direction of travel into the specimen, causing these electrons to return to the entrance surface and exit the specimen. These beam electrons that escape from the specimen are referred to as BSE and constitute an important SEM imaging signal rich in information such as specimen composition, topography, mass thickness and crystallography (Goldstein et al, 2018). It also provides information on the mean atomic weight of the sample (McSween and Huss, 2010).

SE electrons are produced when inelastic scattering by the electron beam expels weakly bound valence electrons (in the case of ionically or covalently bonded materials) or conduction band electrons (in the case of metals) (Goldstein et al, 2018). SE produces higher quality images because they originate closer to the surface of the sample and because more of them are produced per incoming primary electron (McSween and Huss,

2010). SE images have topographical contrast so the morphology of the sample can be analyzed (Goldstein et al., 2018; Hafner, 2015).

#### 1.4.2 Instrumentation

An SEM consists of a source that produces a beam of electrons accelerated to high-energy, a column of electrostatic lenses (usually capacitors), apertures to focus the beam, and one or more detectors. For producing the source beam, two types of electron guns are generally used the thermionic gun and the field emission gun (McSween and Huss, 2010). The thermionic gun is more common and was also the source gun of the SEM equipment used in this research. In this case, electrons are emitted from a heated filament and then accelerated toward an anode. The electrons emerging from the anode are focused into a beam by a set of electrostatic lenses.

In standard operation, a focused beam of high energy electrons is rastered across a rectangular area of a sample and an image is constructed from signals generated in the sample using a computer. Information about the position of the primary beam as a function of time is used to generate the image. The spatial resolution of a scanning electron microscope is governed by a combination of the size of the primary electron beam and size of the interaction volume (McSween and Huss, 2010). Figure 1.6 shows a representative image of industrial diamond taken with the SEM using secondary electrons detection

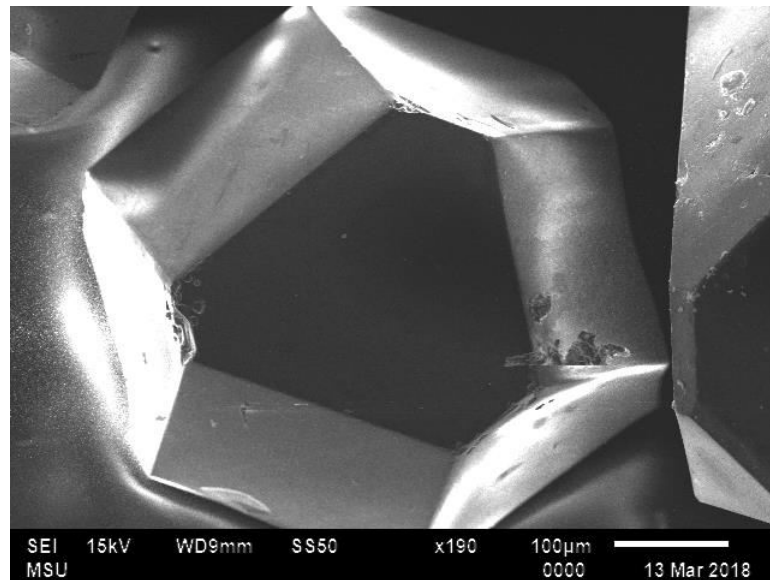


**Figure 1.6.** An industrial diamond viewed under the SEM using SE detection (Stokke, 2018).

### 1.4.3 Applications

Similar to Raman spectroscopy, SEM is a non-destructive technique as well. However, it requires some sample preparation. Samples with low electrical conductivity are first coated with a conducting material before taking data from them. SEM has applications in many fields such as mineralogical and petrologic studies in geology (Reed, 1996), in life sciences for studying tissue damages, neuron activities, etc. (Sanders, 2017), semiconductor and other electronics industries to develop and control the manufacturing process (Holt and Joy, 2013) among several others.

## 1.5 Energy Dispersive X-ray Spectroscopy (EDS)

### 1.5.1 Principle

Section 1.4.1 described the inelastic scattering effect of the incoming electron beam which then ejects valence electrons from the specimen. When the incoming electron beam interacts with an inner shell electron of an atom and consequently ejecting it out of its shell, the atom is left with a vacancy (hole) in that inner orbit. This leaves the atom to be in an excited state. To fill this vacancy, sometimes an outer orbit electron drops to the inner orbit. This transfer of electron from the outer to inner orbit releases an X-ray that has energy equivalent to the difference between the two levels, given by the equation:

$$E_X = E_{in} - E_{out} \quad (3)$$

where subscripts “in” and “out” corresponds to the binding energies of the inner and outer shell electrons, respectively. For each element the difference between its energy levels is unique as well as quantized. Therefore, from the value of this difference in energy the element from which it originates can be identified. The corresponding X-rays are thus called characteristic X-rays (Goldstein et al. 2018). A schematic of the process is shown in Figure 1.6.

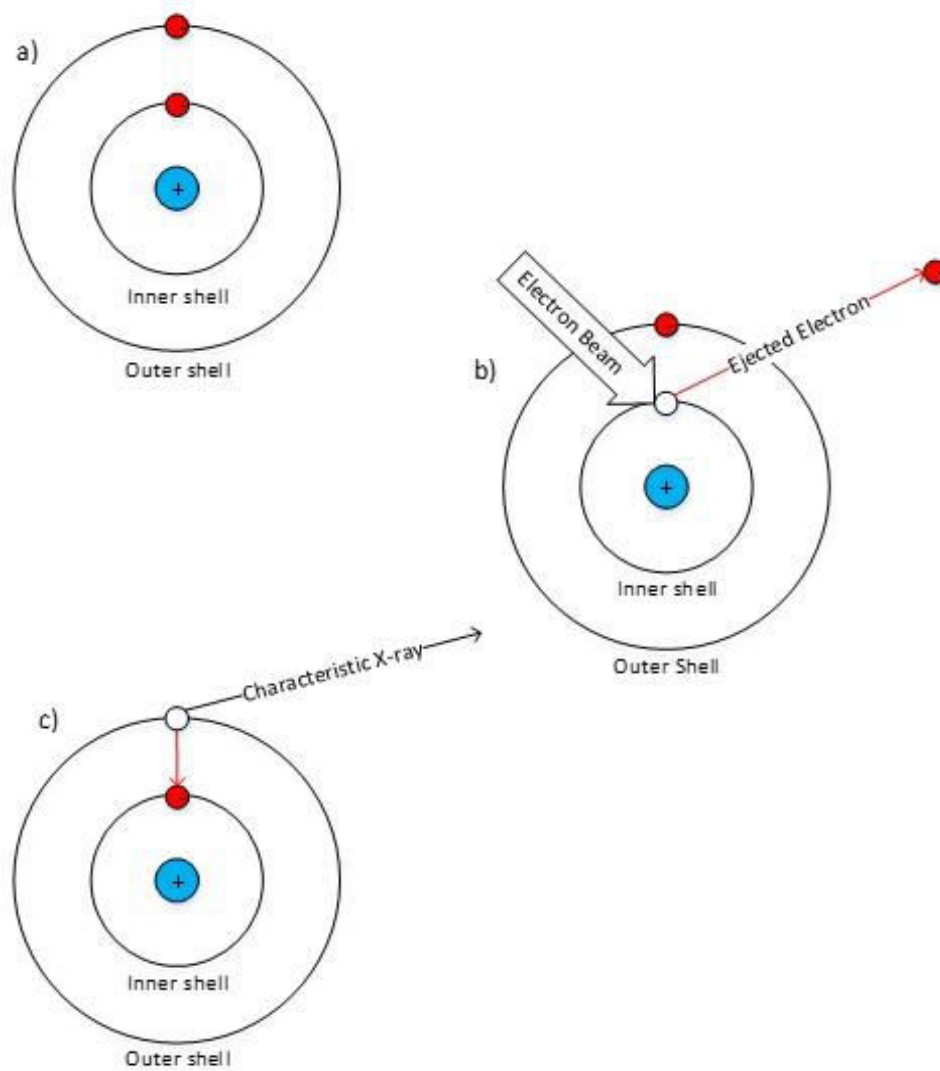


**Figure 1.6.** Diagram illustrating the production of characteristic X-ray from an atom: (a) The atom in its ground state, (b) incoming electron beam ejects an inner shell electron, and (c) outer shell electron jumps down to occupy vacancy thereby releasing X-ray (Stokke, 2018).

### 1.5.2 Instrumentation and applications

The EDS detectors are usually coupled together with SEMs for quantitative chemical analysis. The detectors are typically made of lithium-doped silicon and operated at liquid nitrogen temperature. The electronics recognize each incoming X-ray coming from the specimen and produces a spectrum showing all the X-ray lines present. The software integrated with the system estimates the compositions and gives quantified results for the elements present (McSween and Huss, 2010). Figures 1.7 and 8 show the EDS results coming from industrial diamond.

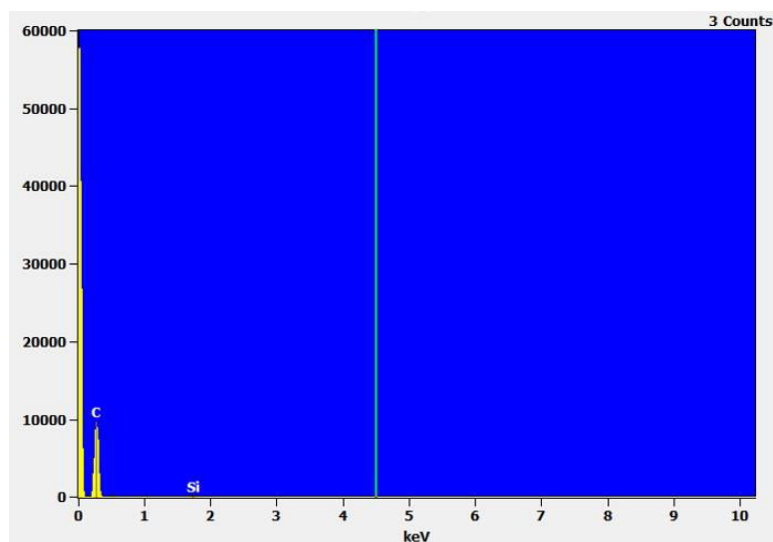


**Figure 1.7.** EDS spectrum for industrial diamond. The x-axis represents the energy of the X-ray (in keV) and y-axis represents the intensity of the signal (in counts) for a given energy. The vertical line at ~4.5 keV is the selection cursor from the data analysis software (Stokke, 2018).

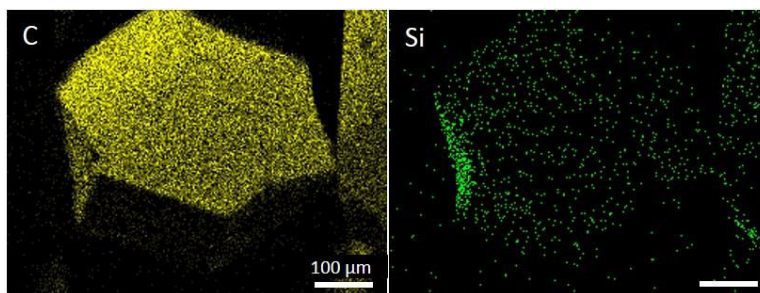


**Figure 1.8.** EDS element maps for industrial diamond (carbon: yellow, silicon: green). Quantitative analysis gives the carbon content to be 99.26 wt. %. The small amount of silicon comes from the wafer on which the diamond is mounted (Stokke, 2018).

## 2. Experimental Methods

In this section, the descriptions of the samples that have been used in this research have been expanded upon, along with the instruments and analytical techniques employed. A micro-Raman spectroscopy system with its software, and a mounted video camera (for sample inspection) was used for obtaining Raman spectra from various parts of the sample. Data was also obtained with the help of an SEM/EDS system and software.

### 2.1 Samples

Two meteoritic samples were chosen: Allende and Bali. They are both carbonaceous chondrites that fall into the ‘Vigarano’- like category (CV) and belong to petrologic type 3. While Allende is notably well-known for being widely studied, Bali however has not been as extensively researched. All CV3 chondrites that have undergone oxidation in their parent bodies (e.g. Kaba, Grosnaja, Axtell) are in-fact classified to be either “Bali-like” ( $CV3_{\text{OXB}}$ ) or “Allende-like” ( $CV3_{\text{OXA}}$ ) meteorites, based on the kind of secondary alterations that their parent bodies experienced (McSween, *Cosmochemistry*, 2010). The samples used in this research were separately contained and preserved under room temperature conditions and did not require any preparation prior to studying.

#### 2.1.1 Allende

One of the samples analyzed was a fragment of the Allende meteorite (Fig 2.1). On February 8, 1969 at 01:05 am, a fireball was observed to blow apart and fall from the

skies near Parral, Chihuahua, Mexico, by the local population. Approximately, 2 tons of meteoritic stones were collected thereafter and some of the largest specimens (5-15 kg) were recovered from the village Pueblito de Allende. The area covered (strewnfield) by the fallen pieces was larger than 300km<sup>2</sup>. Specimens were mostly fragmented, with some stones bearing fusion crusts (Clark et al. 1971).

The Sample (Fig 2.1) was obtained from the online vendor ‘The Meteorite Market’, the owner of which is a recognized member of The Meteoritical Society. Its measured weight was 5.1916 g. The surface was flat with only a few minor abrasions making it compatible to be studied by the SEM/EDS and the Raman systems. Its dimensions were roughly 22.3 mm x 20.6 mm. Several white and dark colored circular inclusions seated within the matrix, were visible with the naked eye.



**Figure 2.1.** Photograph of the Allende meteorite sample used in this research.

### 2.1.2 Bali

The other sample examined in this research was part of the meteorite Bali. The Bali carbonaceous chondrite fell near the Bali mission in Central African Republic, in the country Cameroon, on 22<sup>nd</sup> or 23<sup>rd</sup> November 1907, at around 10:30 am. It was obtained near the Bali mission station on the river Lobaye. The approximate recovered weight of the fallen specimen was 980 g (Grady, M. M., 2000, *Catalogue of Meteorites*).

The fragment of Bali meteorite (Fig 2.2) used in this research was received from a fellow faculty member in the Department of Physics and Astronomy at Minnesota State University, Mankato, who was associated with the NASA Johnson space center. It weighed 66.2 mg and the surface area that was studied had dimensions roughly 6.2 mm x 4.2 mm. The sample does not seem to have been previously polished, however it had a fairly smooth surface. The visible inclusions were primarily white and irregularly shaped; the matrix was mostly grey in color. Like the Allende sample, the flatness of the surface was a definite advantage for data acquisition with the Raman and SEM systems.



**Figure 2.2.** Photograph of the Bali meteoritic sample studied here.

### 2.1.3 Examined regions

Several sites (chondrules, inclusions, and matrix) from the visible surface (Fig 2.1 and 2.2) of both meteorites were chosen to be studied. The samples were inspected under the video camera and the SEM; the sites selected from them for further detailed study were based on their optical visibility, imaging quality under the Raman probe video camera and SEM, as well as their potential for providing quality data. It was also taken into consideration that the selected sites be different from each other based on their preliminary examination (in shape, size, color, etc.). The following figure (Fig. 2.3) shows each sample marked with the sites that were studied. Depending on the area of the site, a number of sub-spots were selected for taking data, the details of which can be found in Section 3. Each site encloses a chondrule, a combination of chondrule-matrix or an inclusion. In this study these sites are referred as “zones” followed by the respective number.

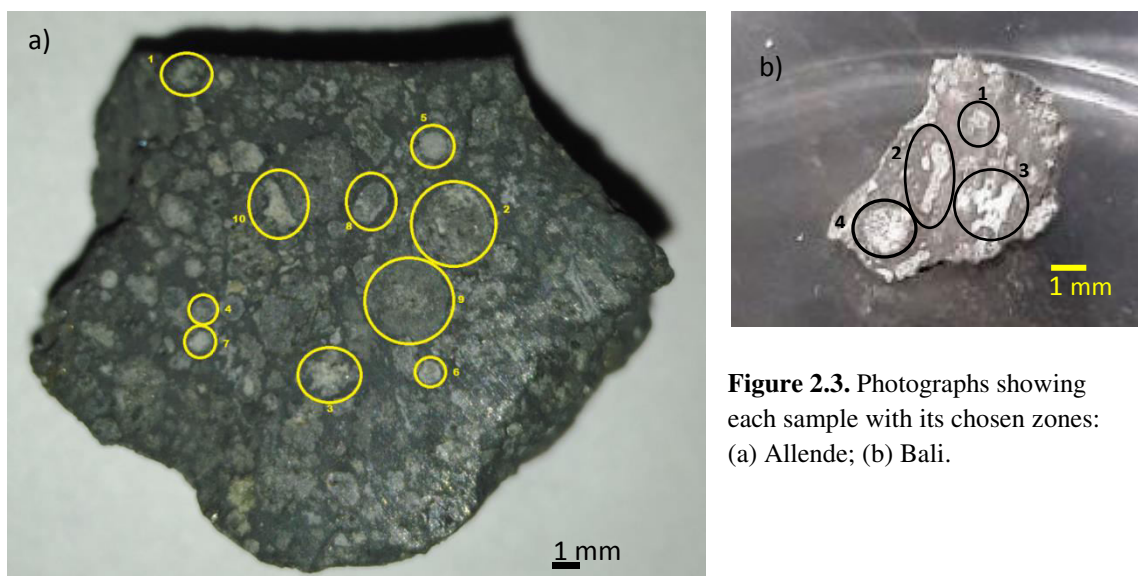


**Figure 2.3.** Photographs showing each sample with its chosen zones: (a) Allende; (b) Bali.

## 2.2 Raman Spectroscopy

### 2.2.1 Experimental Setup and Procedure

The Raman spectroscopy system (Fig. 2.4) used for this research was customized by Dr. Analía Dall'Asén (Department of Physics and Astronomy, MSU). The equipment assembly comprised of the following main components: a semiconductor laser (Coherent Sapphire SF 532 nm), a Raman probe equipped with a video camera, filters, mirrors, lenses, and microscope objective (Renishaw RP20V), a spectrograph (Andor SR-303i-A) with a charge-coupled device (CCD) detector (Andor iDus DU401A-BVF), and a data acquisition computer workstation with spectrometer software (Andor Solis S). Ancillary components of the system included fiber optics cable, stages, and power meters from either Semrock or Thorlabs.

Measurements were taken at room temperature and with a laser power at the sample of approximately 5mW. Following a series of reflection and fine-tuning, the laser beam is channelized and focused on the sample. The Raman probe which transmits the beam onto the sample consisted of a 10X objective lens with a numerical aperture of 0.25. The probe camera connected to computer software displays the sample surface and was used to locate regions to be studied. The beam was focused onto the sample and the scattered signal was collected by the same 10X lens (backscattering configuration). The Rayleigh scattering was filtered out and the Raman signal was directed to the spectrograph and CCD.

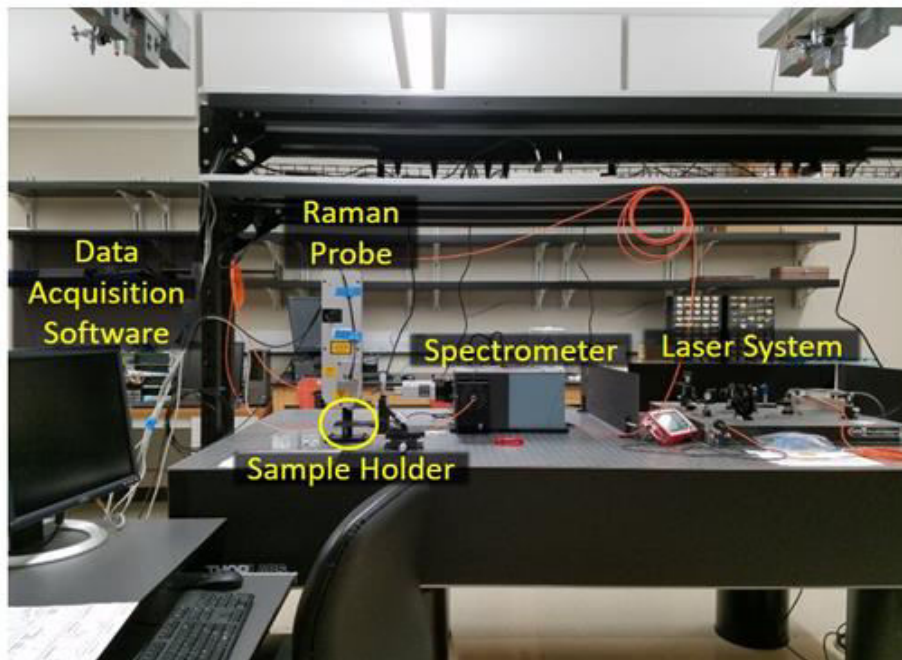


**Figure 2.4.** Photograph of the laboratory setup used for Raman spectroscopic measurements (Stokke, 2018).

After sorting this signal into its respective frequencies, the data was sent to the computer workstation to be compiled with the help of software (Fig. 2.5, image courtesy: Stokke A.R., 2018). Both high- (1200 lines/mm) and low-resolution (600 lines/mm) spectra were taken. The accumulation time was set to one second and ten to one hundred accumulations were taken depending on the resolution and signal-to-noise ratio.

A high power density of the laser spot on the sample may damage/alter the specimen being studied. For the laser power density to be within a risk-free operating threshold, Dall'Asén et al. (2017a) and references therein give a relatively safe value up to  $1300 \text{ W/mm}^2$ . To find the minimum theoretical beam width  $w$ , the following equation can be used:

$$w = \frac{1.22\lambda}{NA} \quad (4)$$

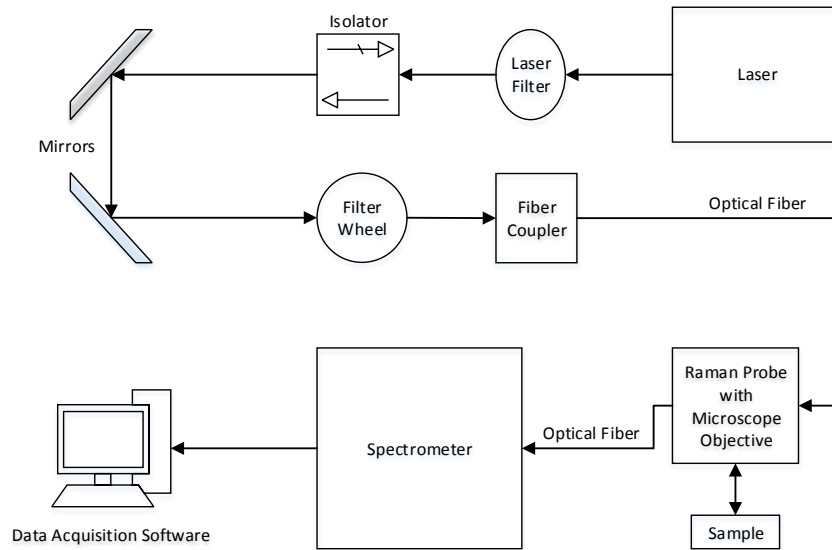


**Figure 2.5.** Schematic of the Raman spectroscopy system (Stokke, 2018).

where  $\lambda$  is the excitation wavelength and NA is the numerical aperture of the objective lens. Using the values given, the minimum beam width  $w$  of this system is  $\sim 2.60 \times 10^{-3}$  mm. Also, the following trivial equation can be used to find the power density  $\sigma$  (power per unit area) of the laser spot on the sample:

$$\sigma = \frac{P}{A} = \frac{P}{\pi r^2} = \frac{4P}{\pi w^2} \quad (5)$$

where  $P$  is the laser power,  $A$  is the cross-sectional area of the beam at the sample, and  $r$  is the radius of the beam at the sample. Plugging in the values from before gives a power density  $\sigma$  of  $\sim 940 \text{ W/mm}^2$ . Imperfections in the system would cause the beam diameter to

be larger than the theoretical value, with estimates from 3 to 5  $\mu\text{m}$ . This would cause the power density to drop, with values ranging from  $\sim 700$  to  $\sim 250$   $\text{W}/\text{mm}^2$ , respectively. However, all the values were still within the upper threshold range as stated previously.

### 2.2.2 Data Acquisition and Analysis

At the computer workstation, the ANDOR Solis S software was used to obtain spectra of the Raman shift (Stokes) wavenumbers. These spectra were then analyzed using the commercial software package, OriginPro 2018. Depending on the shape of the peak in the spectrum data to be fitted, a Lorentzian, Gaussian (Gauss in Origin peak functions) or lognormal in-built function was used. Given below are the equations for each of those functions with their parameters explained:

(i) Gaussian :

$$y = y_0 + \frac{A}{w\sqrt{\frac{\pi}{2}}} e^{-2\frac{(x-x_c)^2}{w^2}} \quad (6)$$

where  $y_0$  is the offset,  $w$  is the peak width,  $x_c$  is the center position of the peak, and  $A$  is the area under the curve. The width is related to the more familiar quantities of standard deviation ( $\sigma$ ) and full width at half maximum (FWHM) by:

$$w = 2\sigma = \frac{FWHM}{\sqrt{2\ln(2)}} \quad (7)$$

Figure 2.6 displays a Gaussian distribution from the OriginPro 2018 software package consisting all of the parameters given in Equations 2.3 and 2.4.

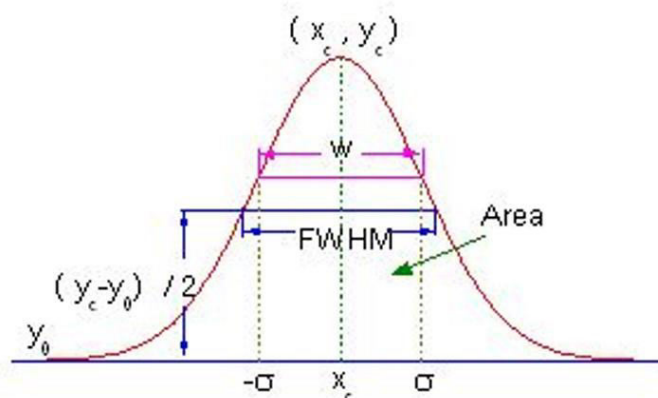


Figure 2.6. Plot of a typical Gaussian distribution.

(ii) Lorentzian:

$$y = y_0 + \frac{2A}{\pi} \frac{w}{4(x - x_c)^2 + w^2} \quad (8)$$

where  $y_0$  = offset,  $x_c$  = center,  $w$  = FWHM,  $A$  = area.

A Lorentzian curve has wider tails than the Gaussian and a narrower FWHM. The Lorentzian fitting was used for the D- and G- band peaks of graphitic carbon in the samples.

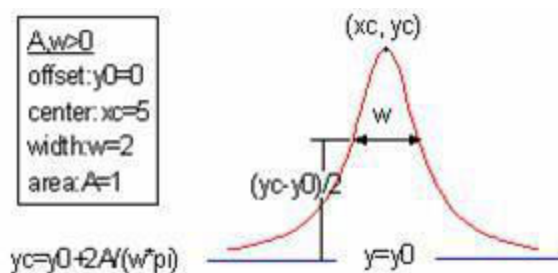
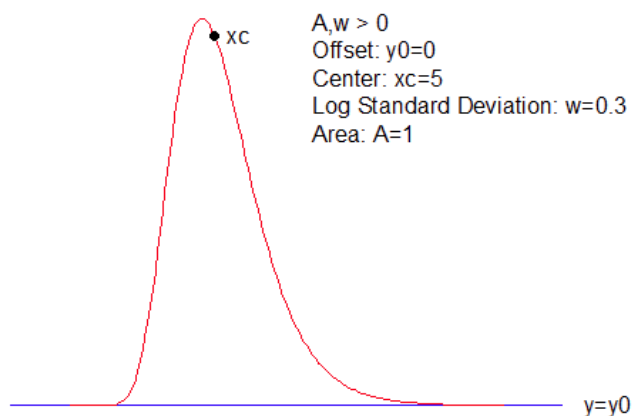


Figure 2.7. Plot of a typical Lorentzian distribution.

(iii) LogNormal:

$$y = y_0 + \frac{A}{\sqrt{2\pi wx}} e^{-\frac{[\ln \frac{x}{x_c}]^2}{2w^2}} \quad (9)$$

where  $y_0$  = offset,  $x_c$  = center,  $w$  = log standard deviation,  $A$  = area. For asymmetric peaks, the LogNormal function was used to fit them.



**Figure 2.8.** Plot showing the LogNormal function.

### 2.2.3 Mineral Identification

Once the Raman shift wavenumbers were determined for the spectra, the peak positions were compared to literature and online databases and libraries to identify the corresponding mineral. Among the databases used was the RRUFF Project ([rruff.info](http://rruff.info)) maintained by the Department of Geosciences at the University of Arizona,

the ‘Mineral Raman Database’ at the University of Parma, Italy, ‘Handbook of Minerals Raman Spectra’ at École normale supérieure de Lyon, France etc.

## **2.3 SEM/EDS**

### **2.3.1 Experimental Setup and Procedure**

The SEM/EDS system used for taking data was located in the Department of Biological Sciences and contained (within a sealed chamber) a scanning electron microscope (JEOL JSM-6510LV) equipped with an energy-dispersive X-ray spectroscopy detector (Thermo Scientific UltraDry). A data acquisition computer workstation with SEM (JEOL SEM Control User Interface 2.23) and EDS (Thermo Fisher Scientific Noran System Six (NSS) 3.0) software was integrated with the hardware.

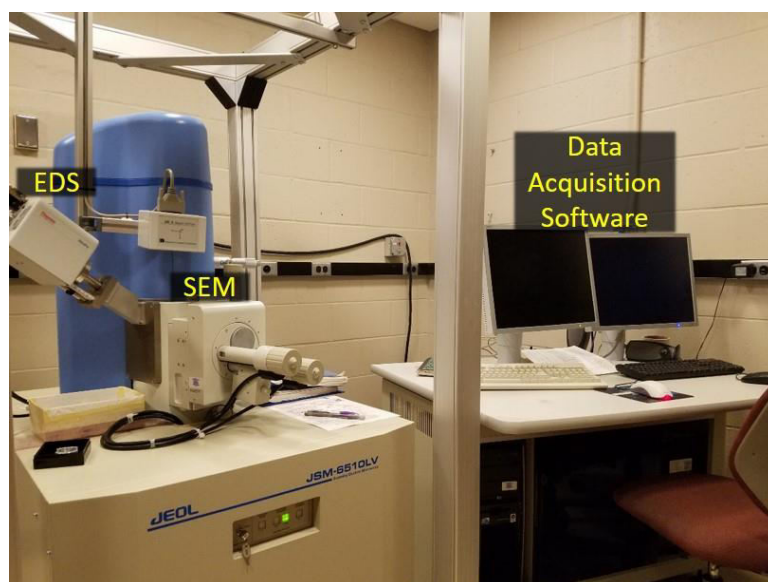


**Figure 2.9.** Photograph showing the laboratory setup for taking SEM/EDS

The sample to be examined was securely placed on a holder using carbon tape for better conductance and adhesion. The holder was mounted within the SEM chamber maintained at a pressure of approximately 10 Pa and room temperature.

Two types of SEM images were acquired, coming from the secondary electrons (SE) and the backscattered electron (BSE) respectively. The two electron image types provide various details about the sample surface. For the secondary electron images, the beam was accelerated at a potential of 15 kV and the working distance (WD) was set to ~10 mm. Secondary electron imaging, being more surface sensitive, provide morphological details of the sample surface up to a depth of about 10 nm. For the BSE imaging, the beam potential was raised to 20 kV while the WD was kept the same. The backscattered images cover more depth of the surface than SE and display the local differences in composition and topography in the form of BSE intensity, with a “contrast mechanism”. The BS electrons are sensitive to the atomic mass of the nuclei they scatter

from. Thus, heavier elements which backscatter more efficiently appear brighter than lighter elements in such images. As an example, Figure 2.10 (a) and (b) respectively show the SE and BSE images, obtained from the same region (zone 1) of the sample Bali illustrating the differences in the kind of details provided by the two imaging techniques.

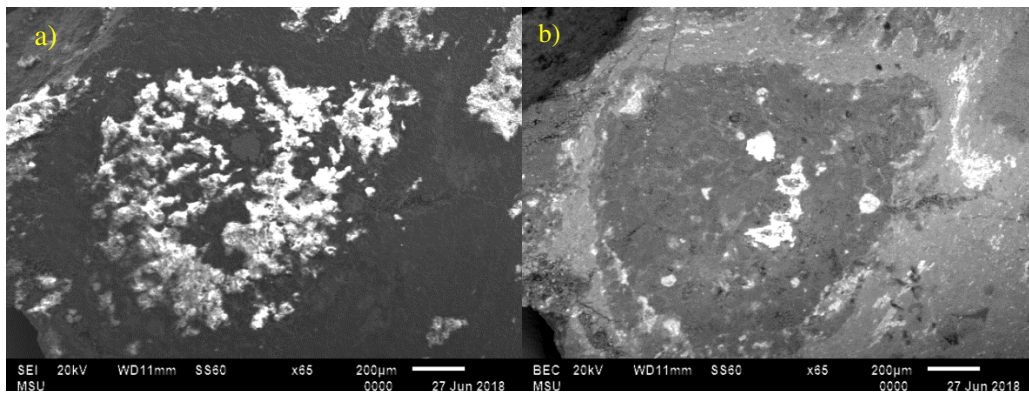


**Figure 2.10.** SEM images of Bali sample zone 1 obtained using: (a) SE detection; and (b) BSE detection.

The spot size parameter controlled a combination of the electron-probe diameter and the illumination current with values ranging from 99 (large diameter and current) to 1 (small diameter and current). Depending on the magnification of the sample surface, the spot size was varied. For lower magnification it was set to be ~60, but when analyzing certain features of the sample at a higher magnification, the spot size was lowered to ~40. Magnification values ranged from 30X to 7000X depending on the structure to be sampled.

### 2.3.2 Data Acquisition and Analysis

After the SE and BSE images are obtained by scanning the intended surface area, the NSS software was implemented to acquire elemental maps from the same region. The software had peak identification techniques pre-programmed into the system to match the incoming X-ray spectra from the sample to its database in order to identify the present elements. It also quantitatively tabulated the elemental compositions by their percentages by weight.

## 3. Results and Data Analysis

This chapter reports the identified and unidentified minerals obtained from Raman spectroscopy of the samples along with their SEM/EDS findings. Representative Raman spectra and SEM images along with the elemental maps obtained from EDS with percentages by weight are shown.

### 3.1 Allende

#### 3.1.1 Raman spectroscopy

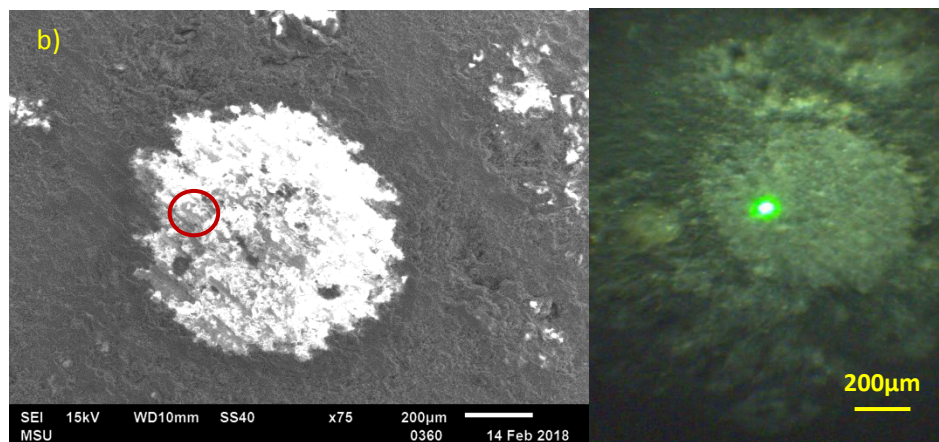
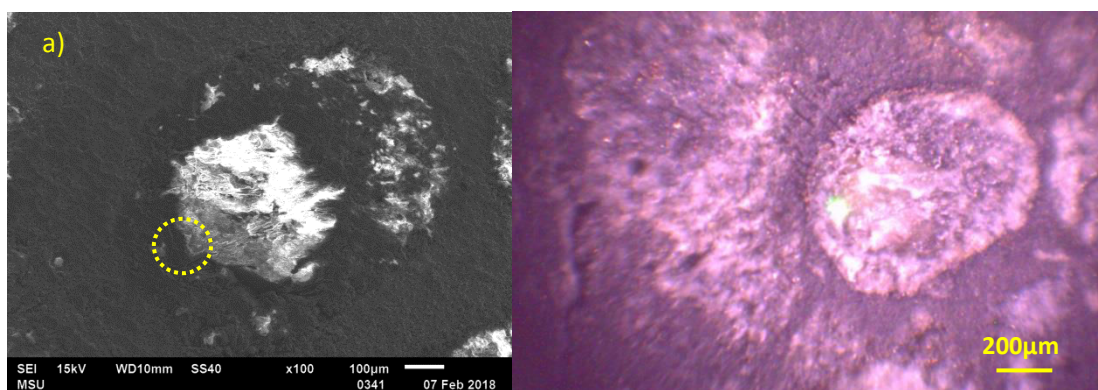
A number of minerals were identified in the sample from their corresponding Raman spectra. Among them olivine, pyroxene and graphitic carbon were ubiquitous throughout the sample and followed certain trends (discussed later). Further analyses of the peaks coming from these minerals reveal important details about the sample and its parent body. For example, the D- and G- bands arising due to the presence of defected graphite in the sample are used to obtain information such as the degree of “amorphization” undergone by the parent body (Ferrari and Robertson, 2006) and the peak metamorphic temperature (PMT) of their parent body (Busemann, 2007; Homma, 2015) etc. The olivine doublet peak positions were indicative of the percentage composition (Kuebler *et al.*, 2006) of the type of olivine: fayalite ( $\text{Fe}_2\text{SiO}_4$ ) and forsterite ( $\text{Mg}_2\text{SiO}_4$ ). As presented in data analysis, the olivine peaks from this sample came from a mixture of fayalite and forsterite, with forsterite being dominantly present. Similarly, peak position analysis of the pyroxenes also tells us the composition of the pyroxene

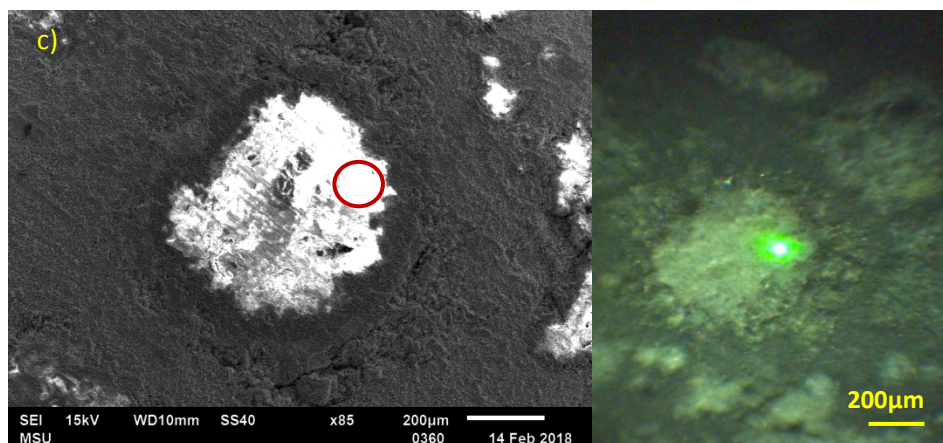
present therein (Huang *et al.*, 2000; Tribuadino *et al.*, 2012). In this sample the pyroxenes were either a combination of diopside-clinoenstatite ( $\text{Di}_x\text{En}_y$ ) or a combination of enstatite-ferrosilite ( $\text{En}_a\text{Fs}_b$ ). The chemical formulae of enstatite, diopside and ferrosilite are  $\text{MgSiO}_3$ ,  $\text{MgCaSi}_2\text{O}_6$  and  $\text{FeSiO}_3$  respectively.

Figure 3.1 shows representative SEM and Raman probe video camera images of some of the studied zones. The spots from where the Raman spectra were obtained are shown with the laser beam in the video camera images and have been encircled on the SEM images. For each spectrum, the main mineral is highlighted by the peaks that are labelled, with no labels on peaks coming from other minerals. The first spectrum (Fig. 3.2a) exhibits graphitic carbon, sampled from a spot in the matrix. As shown, the D-band's position is  $1355\text{ cm}^{-1}$  and the G-band is located at  $1605\text{ cm}^{-1}$ . The D-band results from defects in the crystal structure while the G-band comes from the stretching of C-C bonds (Dall'Asén *et al.*, 2017). Figure 3.2b shows an olivine spectrum with peaks at  $824\text{ cm}^{-1}$  (DB1) and  $856\text{ cm}^{-1}$  (DB2), these features arise from coupled symmetric and asymmetric stretching vibrational modes of the constituent  $\text{SiO}_4$  tetrahedra (Kuebler *et al.*, 2006). From the peak positions it is clear that this spectrum corresponds to 100% forsterite. It was taken from zone #7, spot 2 which lies within the chondrule area.

The pyroxene spectrum shown in Fig. 3.2c is a diopside-enstatite combination (Di-En) type of approximate composition  $\text{Di}_{15}\text{En}_{85}$ , as is evident from the peaks at  $339\text{ cm}^{-1}$ ,  $401\text{ cm}^{-1}$ ,  $666\text{ cm}^{-1}$ ,  $685\text{ cm}^{-1}$ ,  $1013\text{ cm}^{-1}$  and  $1033\text{ cm}^{-1}$ . This spectrum is taken from zone 4, spot 1 which lies at the chondrule-matrix boundary. As discussed earlier, depending on its composition, pyroxene shows characteristic Raman bands at various

peak positions. The variations in wavenumber are related to the straightening of the tetrahedral chains and the corresponding changes in the Si-O bond lengths and O-Si-O angles caused by substitution of Fe for Mg (Huang *et al.*, 2000). Quartz was also found in the sample, its spectrum with peak position is shown in Figure 3.2d





**Figure 3.1** SE images and Raman video probe images of the Allende sample obtained from the encircled spots: (a) zone 4, spot 1; (b) zone 5, spot 2; and (c) zone 7, spot 2.

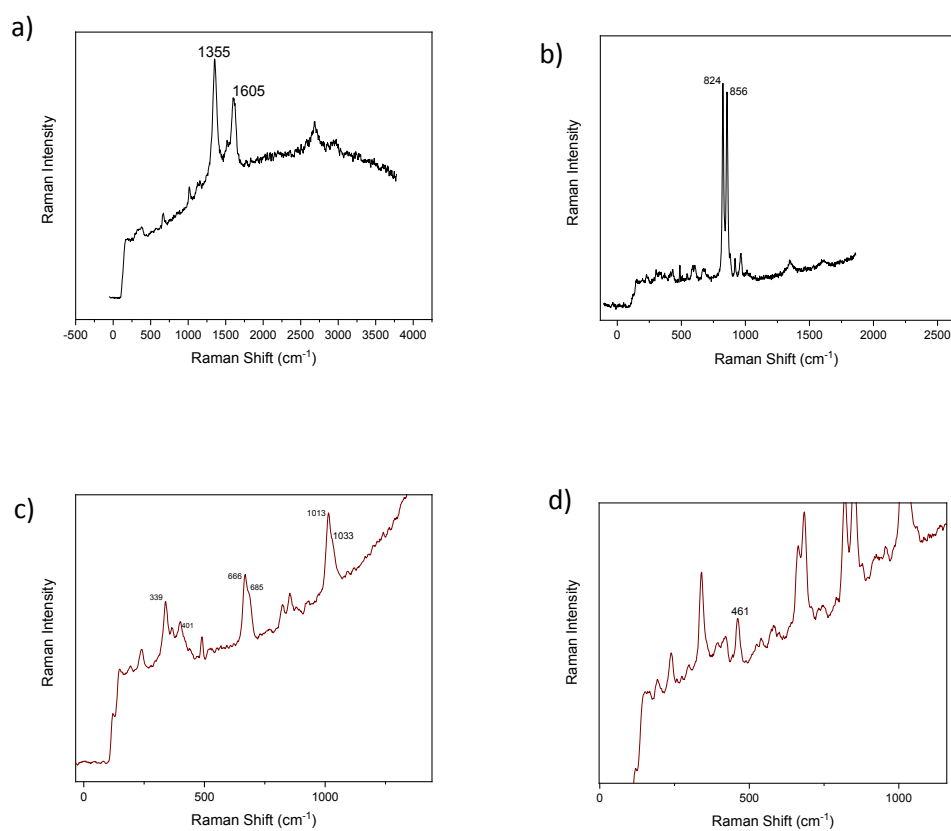


**Figure 3.2.** Representative Raman spectra of main materials obtained from the Allende sample: a) graphitic carbon (matrix), b) olivine (zone 7 spot 2), c) pyroxene (zone 4 spot 1), and d) quartz (zone 5 spot 2).

The olivine spectra were fitted using a Lorentzian function and the peak numbers obtained thereafter was compared to the analytical study done by Kuebler *et al.*, (2006) to determine the fayalite-forsterite percentages. From the obtained results, it was seen that the highest to lowest forsterite (Fo) percentage by weight were Fo<sub>100</sub> and Fo<sub>20</sub> respectively, with majority of the data showing a higher percentage of forsterite by weight. The forsterite (Mg-rich olivine) was replaced by the Fe-rich fayalite where the forsterite was absent.

For the pyroxene spectra, the peak positions were obtained by Lorentzian, lognormal or Gaussian fittings. To identify the type (or combination) of pyroxene, the works of Huang *et al.*, (2000) and Tribuadino *et al.* (2012) were referred. Comparing the obtained peak positions to those literatures, it was seen that the pyroxene present was mostly rich in enstatite, with some of the enstatite being replaced by either diopside or ferrosilite. Similar to olivine, enstatite is Mg-rich silicate; and where enstatite was absent, some of the Mg was replaced by either Ca (resulting in diopside) or with Fe (ferrosilite). The highest diopside-clinoenstatite ratio found from the peak positions was ~Di<sub>80</sub>En<sub>20</sub> while the lowest was ~Di<sub>15</sub>En<sub>85</sub>. The highest and lowest enstatite-ferrosilite ratios were ~En<sub>90</sub>Fs<sub>10</sub> and ~En<sub>78</sub>Fs<sub>22</sub> respectively.

The probable causes and implications for the above observations are discussed in Section 4 along with carbon peak parameters and PMT values.

### 3.1.2 SEM and EDS

Figures 3.3 through 3.16 show some of the well-defined SEM images with the corresponding elemental maps from EDS accompanying some of them. In both types of SEM images, a clear distinction between the matrix and inclusion (chondrule, CAI, etc.) is possible to see by the contrast mechanism. These images also exhibit other details such as the topography and the relative position of elements. Physical structures such as rims or veins can also be observed.

Some general trends and correlations were observed in all the zones studied. O and Si were present nearly throughout the entire region with only a few exceptions. Fe, S and Ni were abundant in the matrix and deficient within the inclusion. Mg on the other hand, was present more within the inclusion than in the matrix. Several Ca-Al patches were scattered in the matrix or within the inclusion. S formed rims around some of the inclusions. For certain C-rich spots that were sampled, the high resolution EDS maps show that the carbon therein is present exclusively with almost no accompanying elements (except O and Si). These carbon structures appear to be flat layer-like in the secondary electron (SE) images. Clusters of Fe-S, Fe-Ni, or Fe-Ni-S were also present in some of the zones.

Table 3.1 gives a list of all the elements found in the sample in this study (using 25 measurements), the major elements were O, Mg, Si and Fe; the minor elements were C, S, Ni and Ca; and the trace elements were Al, Cr, Na, Mn and P.

Allende CV3 chondrite											
Element (wt. %)	O	Fe	Si	Mg	C	S	Ni	Ca	Al	Na	Cr
Findings in this study	36.62-25.58	29.36-20.23	16.13-13.73	16.74-11.12	9.41-2.39	3.13-1.43	2.30-1.63	3.75-1.44	3.77-1.01	1.38-0.29	0.88-0.56
Hutchinson, 2004	34.8	23.5	15.6	14.5	0.56	2.2	1.34	1.90	1.75	0.33	0.360

**Table 3.1.** List of the elements and their wt. % found in the Allende sample along with the values reported in literature for CV chondrites.

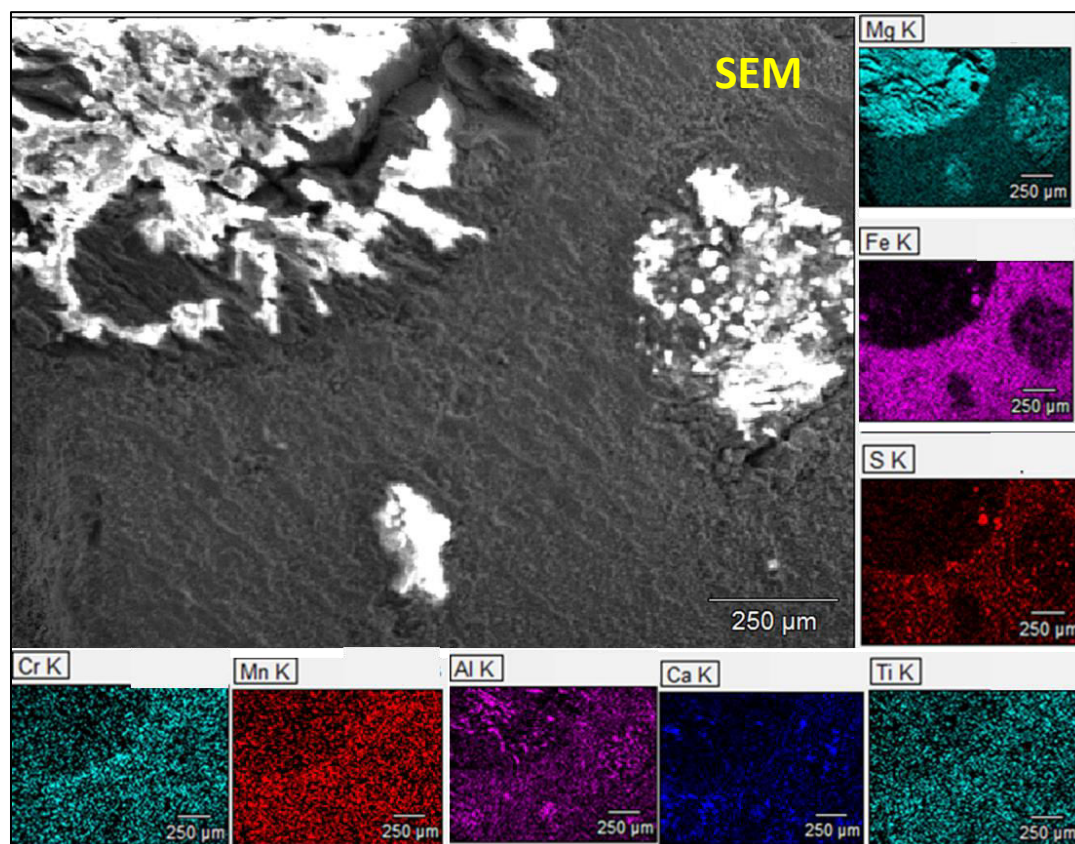


**Figure 3.3.** SEM image using secondary electrons (SE) detection and EDS maps from a selected area (zone 1) of Allende meteorite sample at a magnification of 80X. The Mg/Fe correlation is seen in the EDS maps of the respective elements: Mg, Fe, S, Ti, Al, Mn, Ca and Cr.

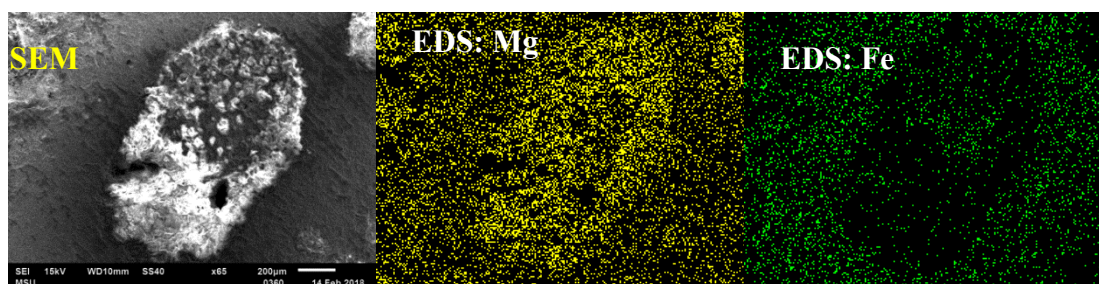


**Figure 3.4.** SEM image using secondary electrons (SE) detection and EDS maps of Mg and Fe of zone 8.

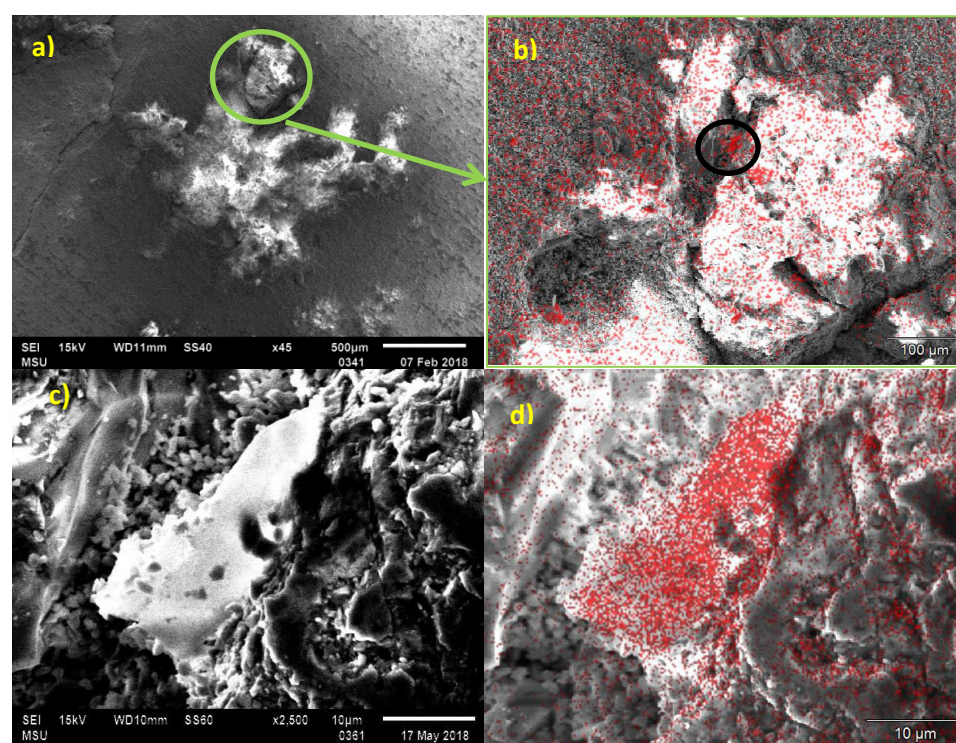


**Figure 3.5** (a) SEM image of zone 3, magnification 45X, (b) SEM image with the EDS mapping of C on it viewed at 250X, the black circle encloses the region zoomed in further, (c) SEM image of the encircled C-rich region viewed at 2500X, (d) EDS map of C on the zoomed area 2500X.

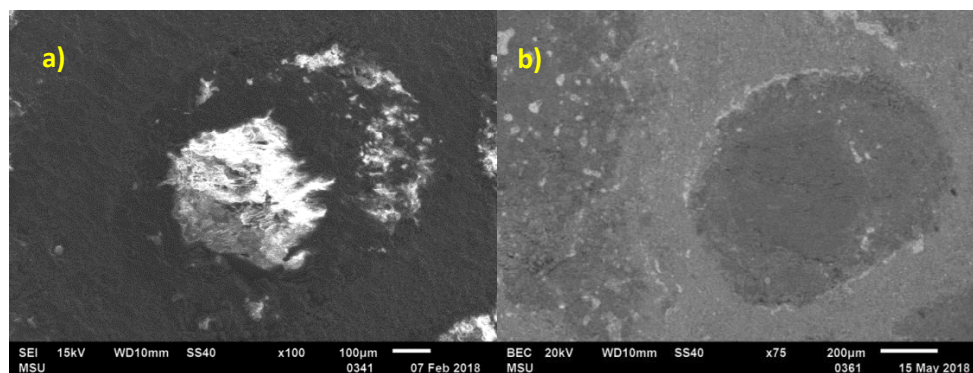


**Figure 3.6.** (a) SE imaging of zone #4, 100X; (b) BSE image of zone #4 at 75X.

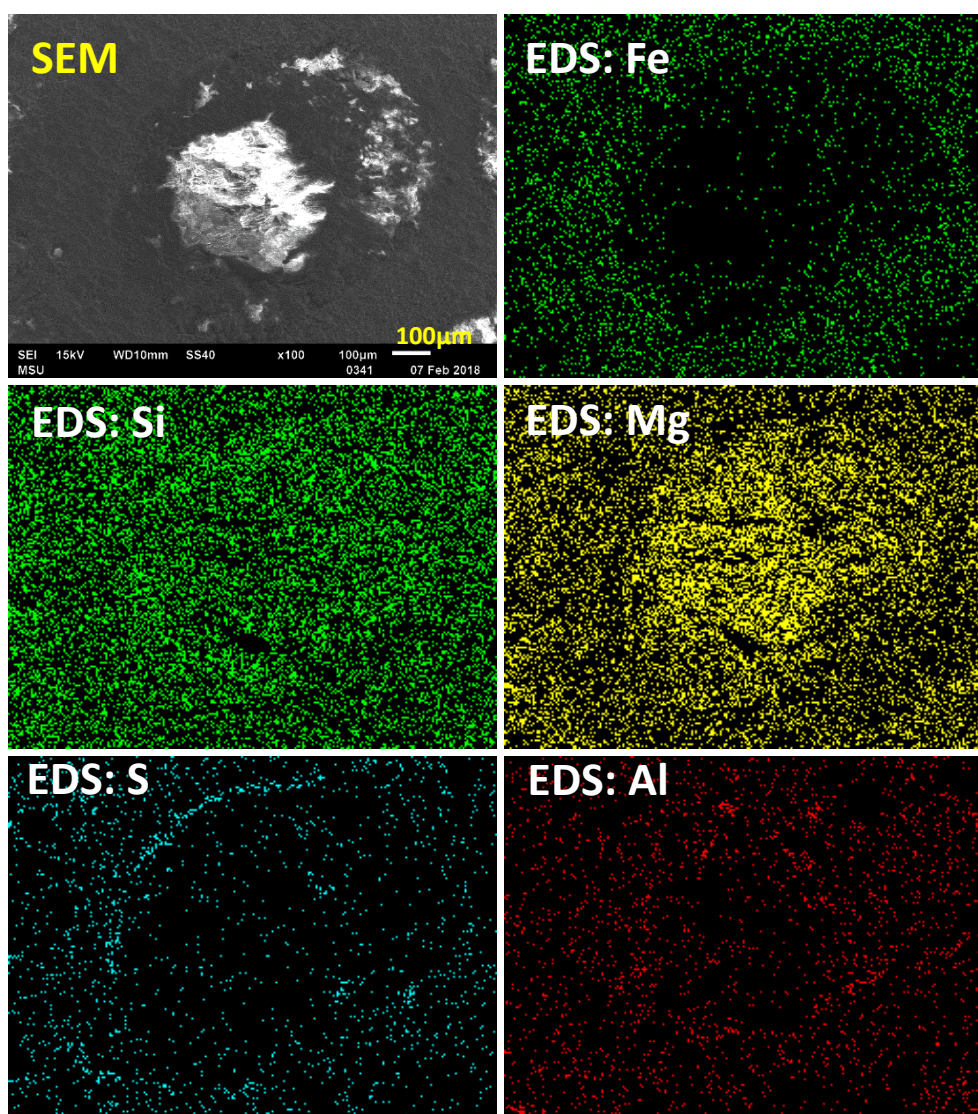


**Figure 3.7.** SEM/EDS Images of Allende zone 4 whole 100X; showing the SEM image and EDS maps of the elements: Mg, Fe, S, Si and Al.

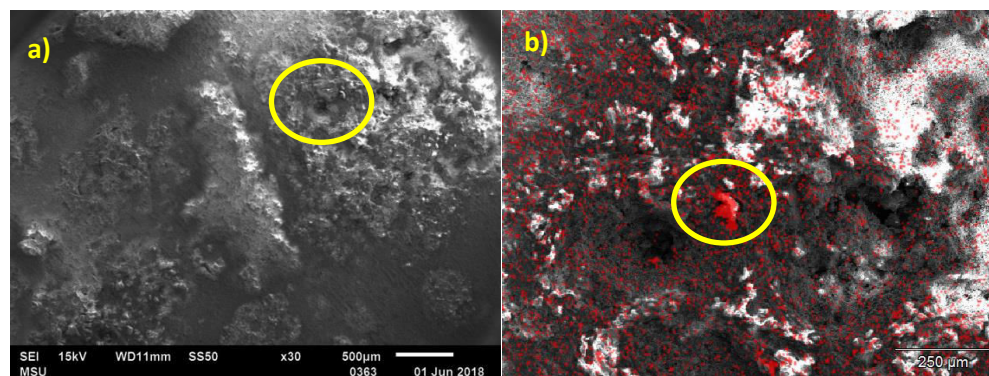


**Figure 3.8.** (a) Zone 10 viewed under the SE imaging at 30X, the circled region contained a C-rich spot; (b) SE image of the circled area with the EDS mapping of C on it.

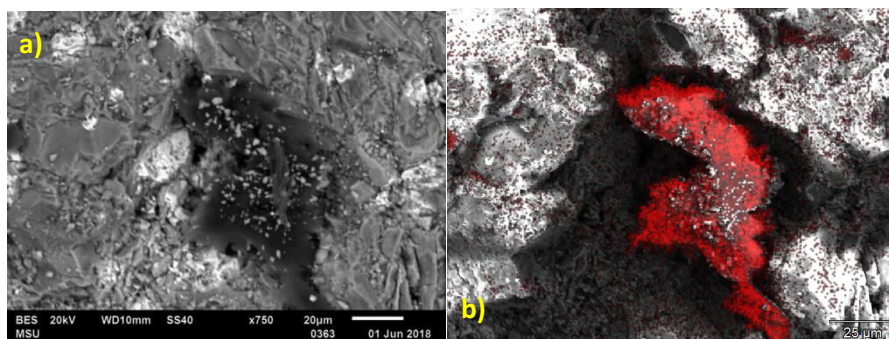


**Figure 3.9.** (a) BS image showing the smooth C-rich area (circled in Fig. 3.7b) with its rocky surroundings; (b) SE image with EDS map of C of the same region; both at 750X

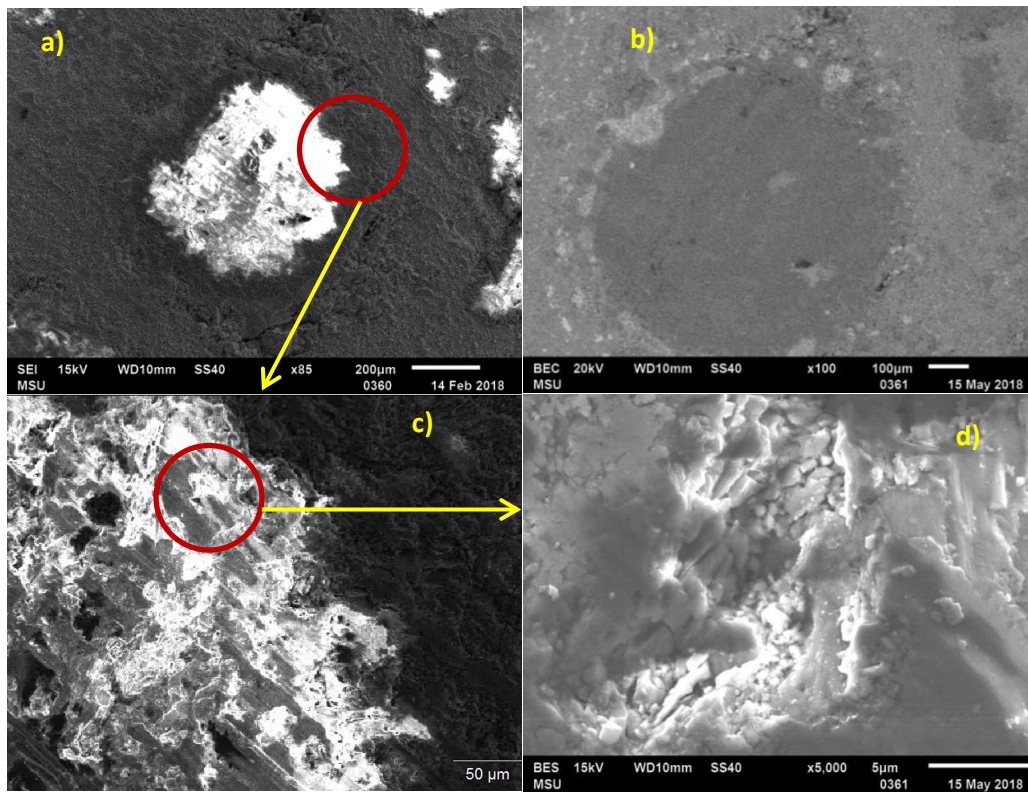


**Figure 3.10** (a) SE image of zone 7 at 85X; (b) BSE image of zone 7 at 100X; (c) higher magnification SE image of region in circle 1; (d) A C-rich spot was found within circle 2 which was then viewed at 5000X BS, to investigate the underlying structure.

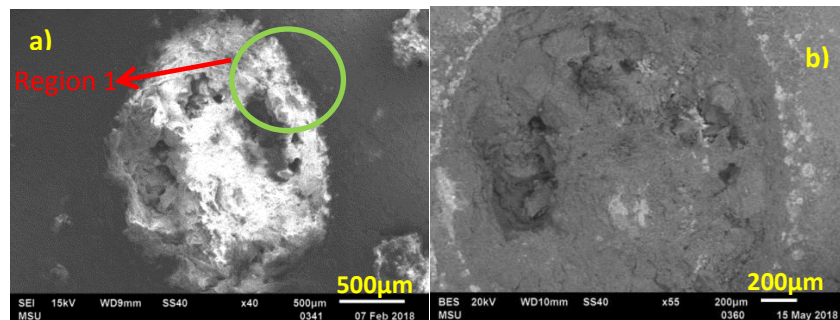


**Figure 3.11**(a) SE image of zone 2 at 40X, (b) BSE image of the same zone at 55X; NOTE: although some areas get excluded in the 55X BSE image, the differences in the features shown by BS electrons are notable when comparing it to the SE image.

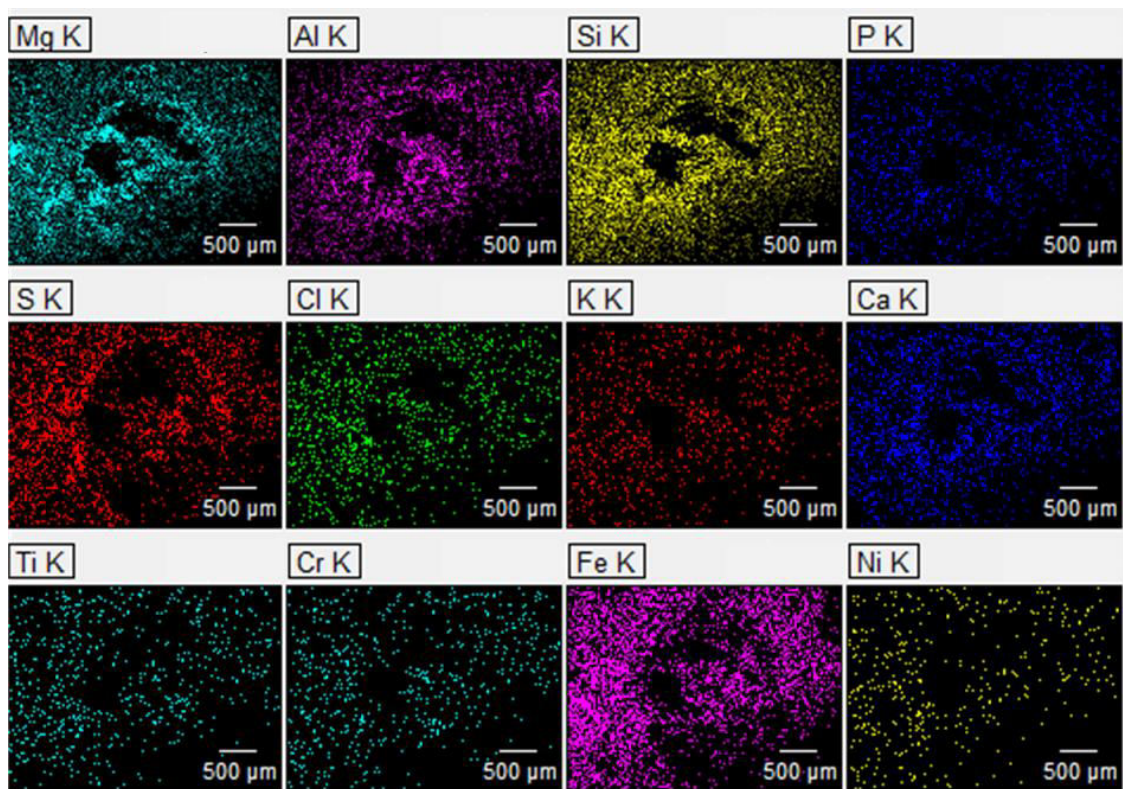


**Figure 3.12** EDS maps of some of the elements present in zone 2. A rim of S is seen to surround the chondrule.

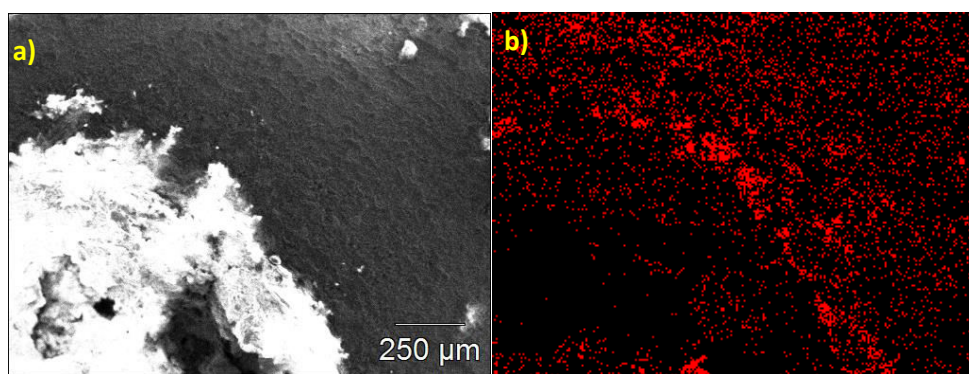


**Figure 3.13** (a) SE image of Region 1 (encircled in Fig. 3.11a) of zone 2 further magnified (b) The EDS map of S showing the rim at the region.

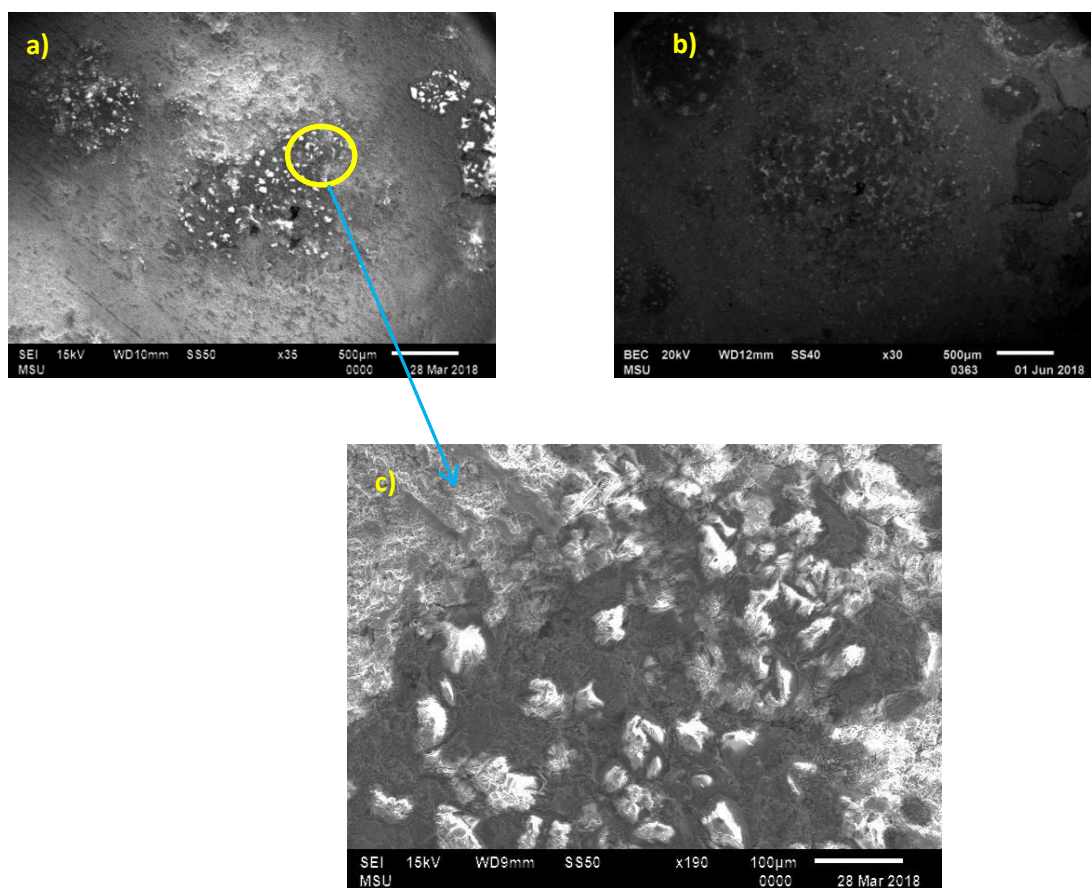


**Figure 3.14** (a) SE image of zone 9 at 35X; (b) BSE image of zone 9 at 30X; (c) higher magnification SE image of circled area in (a) at X190.

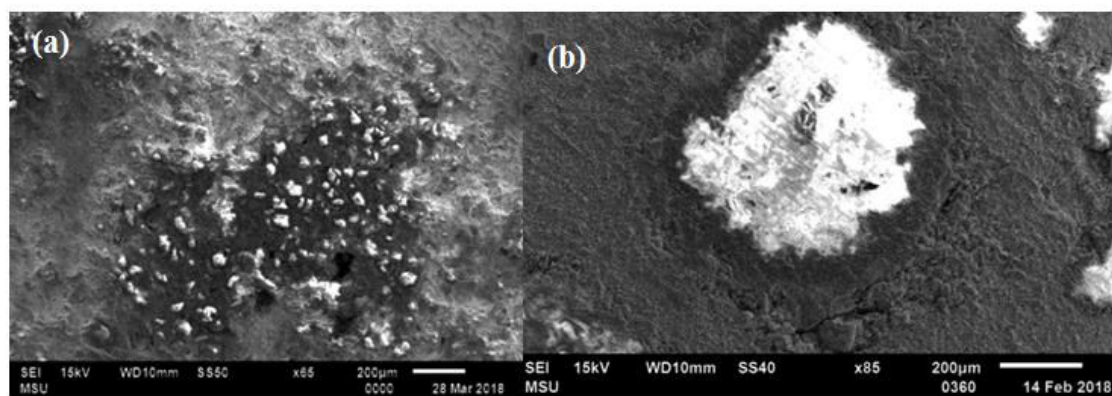


**Figure 3.15.** SEM images of the Allende sample: (a) Inclusion 9: a porphyritic chondrule; (b) Inclusion 6: with several parallel lines visible across the chondrule (white region).

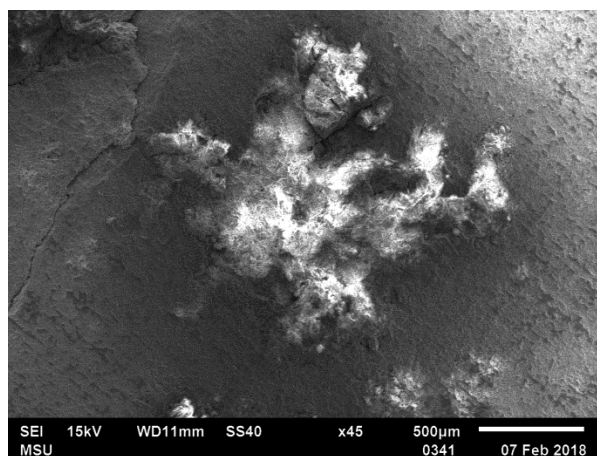


**Figure 3.16.** SEM image of the Allende sample inclusion 3.

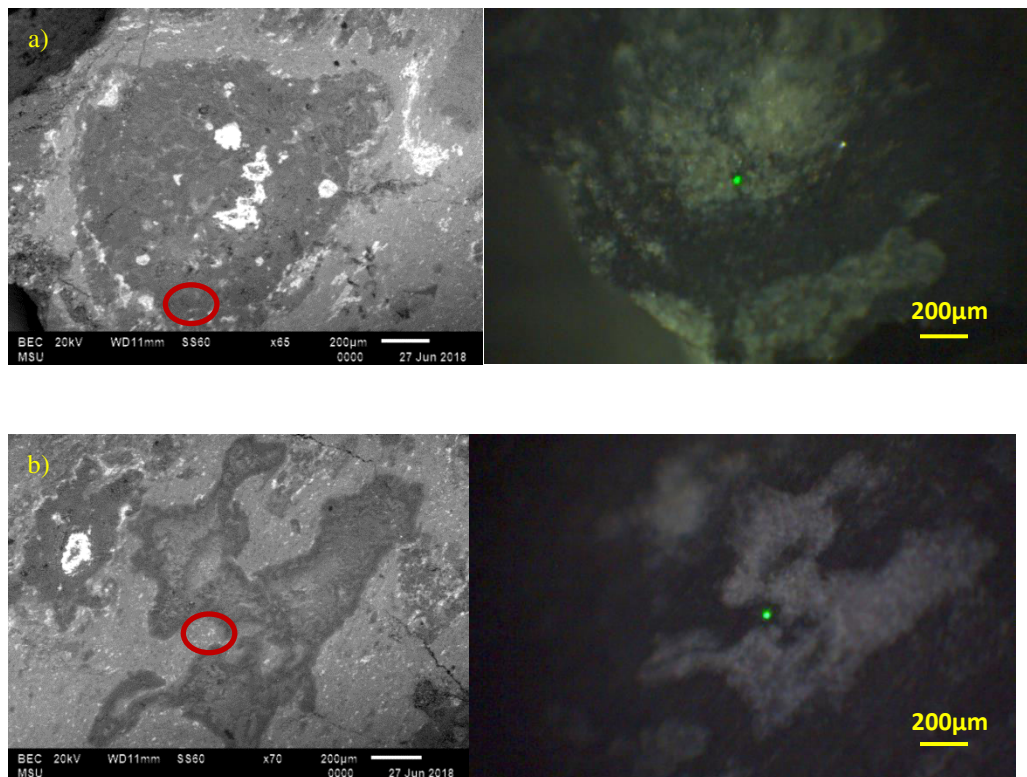
## 3.2 Bali

### 3.2.1 Raman Spectroscopy

Figure 3.18 (a) through (e) shows representative Raman spectra of the Bali meteoritic sample coming from several zones. The zones along with circles enclosing the spot marked by the laser dot are shown in Figure 3.14. In general, no pyroxene peaks could be observed in the sample, however the olivine peak analysis showed a higher Fe content than the Allende sample. Graphitic carbon and olivine were also present along with some unidentifiable minerals. This sample also had a high fluorescence making data acquisition and peak identification much difficult. Additionally, the data had low signal-to-noise ratio. Due to these reasons, a clear identification of the mineral(s) for several spectra was not achieved. However, based on the prominent peak positions and their widths in those spectra, along with the composition of the spot (from EDS), they were compared to some possible mineral spectra from literature and online databases. One

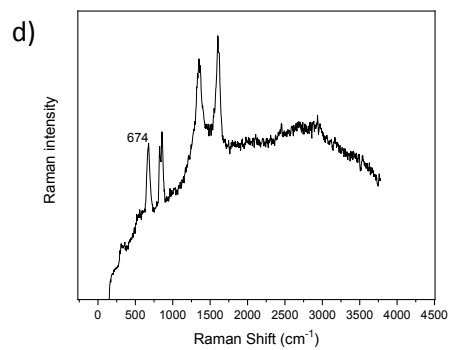
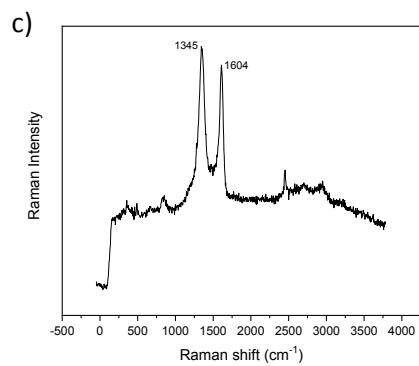
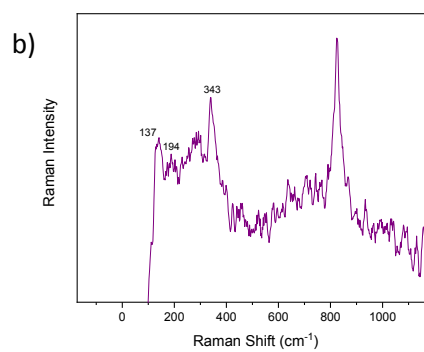
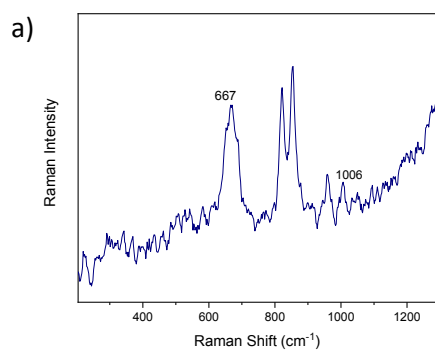
such example is of larnite ( $\text{Ca}_2(\text{SiO})_4$ ), spectrum shown in Fig.3.2.1(a), the data was obtained from zone 1 spot 2. This spot does include the elements of that mineral obtained from the EDS maps. Also, the widths, positions and respective intensities of the main peaks of the database spectrum (RRUFF ID: R070530), match with the sample data spectrum. Another mineral with similar possibilities of matching spectra (RRUFF ID: R070671) from this sample include: awaruite (Fe-Ni alloy).

At least two minerals were unidentifiable from this sample. The peaks at  $488\text{ cm}^{-1}$  and  $2448\text{ cm}^{-1}$  seem to be present together in several sample, therefore, they could be originating from a particular mineral or combination of the same minerals. Another peak at  $825\text{ cm}^{-1}$  also remained unidentified.





**Figure 3.17.** SE images and Raman video probe images of Bali: (a) zone 1 with spot 1 encircled; (b) zone 3 with spot 3 encircled; (c) zone 2 with spots 1, 2 and 3 encircled. For zone 3 only one representative Raman video probe image is shown with the laser point within spot 3.



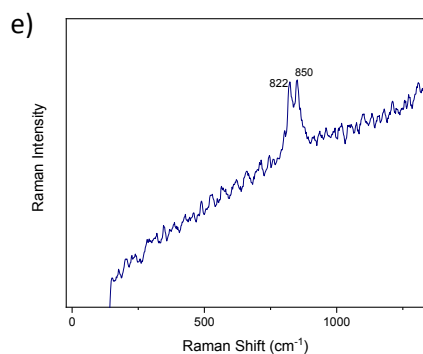


**Figure 3.18.** Representative Raman spectra found in the Bali sample: a) larnite from zone 2, spot 3; b) awaruite from zone 2 spot 1 ; c) graphitic carbon from zone 2 spot 2; d) magnetite-like mineral from zone 1 spot 2 ; e) olivine from zone 3 spot 3.

The Raman spectrum of magnetite shows the peak slightly to the right of the generally accepted value 671  $\text{cm}^{-1}$ . This peak shift has been reported in other works (de Faria *et al.*, 1998) as a transition taking place between magnetite and hematite due to heating from the laser beam. However, since the laser beam was kept well within the operational threshold, no conclusive evidence was found that this peak shift is indeed from the beam affecting the sample. As with the other sample, the olivine doublet peak positions of Bali were also analyzed and compared to literature (Dall'Asen *et al.*, 2017). The analysis results show that the olivine in this sample was also mostly forsterite. The highest and lowest forsterite compositions being  $\text{Fo}_{90}$  and  $\text{Fo}_{10}$  respectively and most of the data were  $\text{Fo}_{80}$  in composition.

### 3.2.2 SEM and EDS

The SEM/EDS data of the Bali meteoritic sample show a wide variation in the combinations of elements that are present. Figure 3.19 through 3.26 show some well-defined SEM images and their EDS maps. By simple inspection, it is possible to distinguish the matrix from the rest of the zone. The sample appeared to be composed of several “melts”, crystals and other tiny zones embedded in the matrix. It was not clear whether any of those zones were chondrules. Several elements show a visibly clear trend of either being present together with another element (such as Fe-Ni or Fe-Ni-S) or being complementary in location with a different element (e.g. Fe/Mg) in several locations throughout the sample. Carbon was mostly homogeneously present throughout the sample, although several high-resolution data taken from some selected regions show the exclusive presence of only a few elements such as Ca and Al, or Fe and Ni; with all other elements being absent. Interestingly, trace elements such as Ti, Mn and Cr also appeared to be clustered together in certain spots, sometimes present together with Fe, Ni and S.

Table 3.2 gives a list of the main elements found in the sample (using 16 measurements) with its weight percentage ranges. The major elements were O, Fe, Si and Mg; the minor elements were C, S, Ni and Ca; and the trace elements were Al, Na, Cr, P, Mn, Ti and Ta.

Bali CV3 chondrite													
Element (wt. %)	O	Fe	Si	Mg	C	S	Ni	Ca	Al	Na	Cr	P	Ti
Findings in this study	35.96 -32.91	27.68 -18.67	13.05 -12.41	12.31 -10.24	12.07 -8.09	1.93 -1.42	1.32 - 0.88	3.82 -1.53	5.97 -0.93	0.78 -0.49	0.43 - 0.30	0.08 - 0.07	0.18 - 0.09
Hutchinson, 2004	34.8	23.5	15.6	14.5	0.56	2.2	1.34	1.90	1.75	0.33	0.360	0.099	0.098

**Table 3.2.** List of the elements and their wt. % found in the Bali sample along with the values reported in literature for CV chondrites.

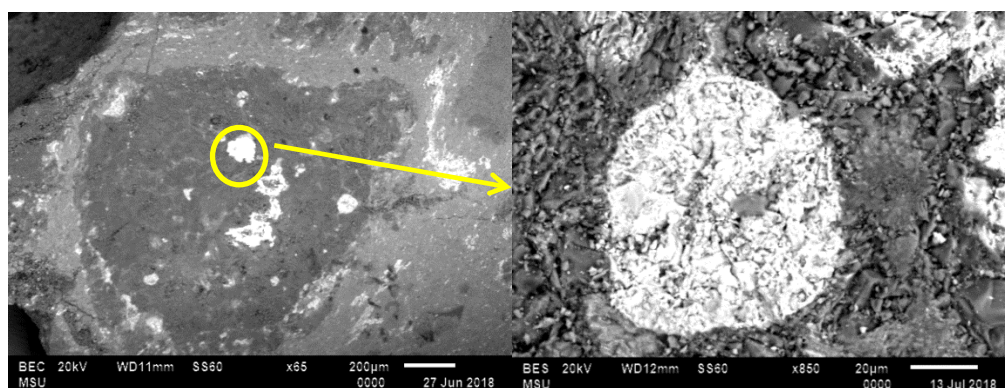


**Figure 3.19.** Zone 1 BS image with a circular Fe-Ni area highlighted.

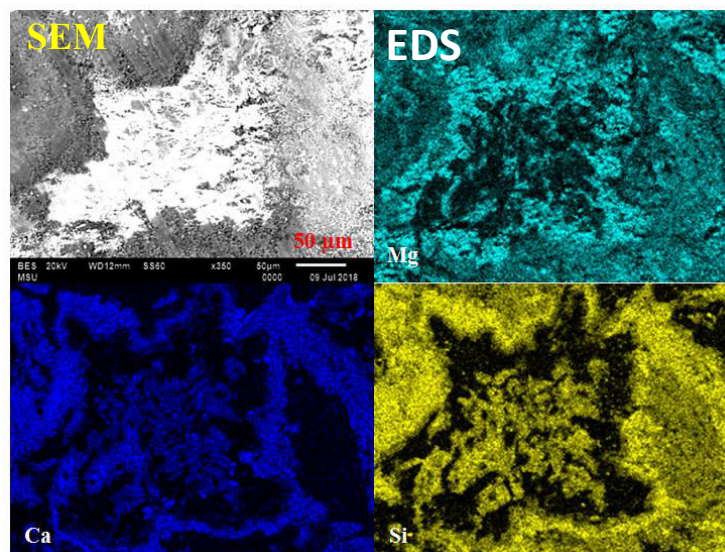


**Figure 3.20.** High-resolution (350X) BE image taken from the interior of inclusion 3 with the EDS maps showing the geometric structures in which the elements are present together.

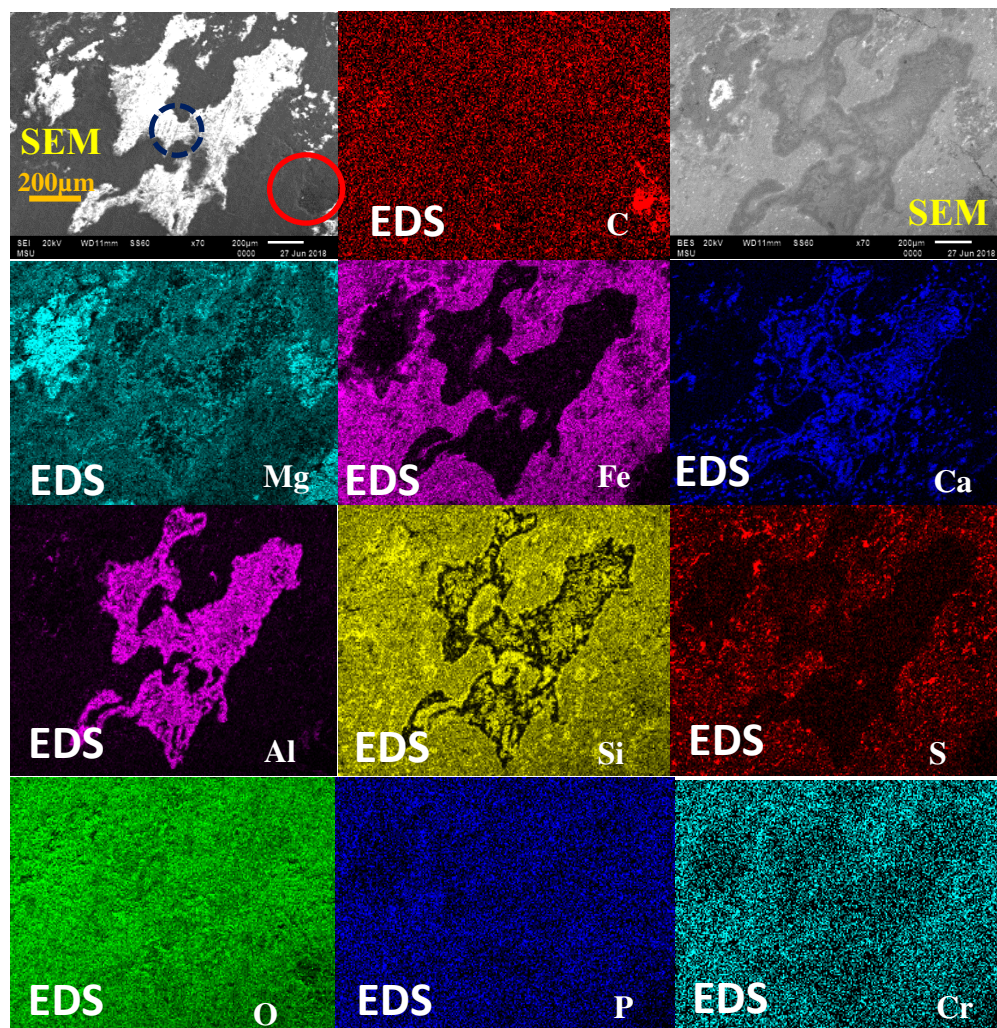


**Figure 3.21.** SEM images: SE (top left corner), BSE (top right corner) and EDS maps of elements of zone 3; the red encircled region shows a dense C-concentration, as seen from the EDS map of C.

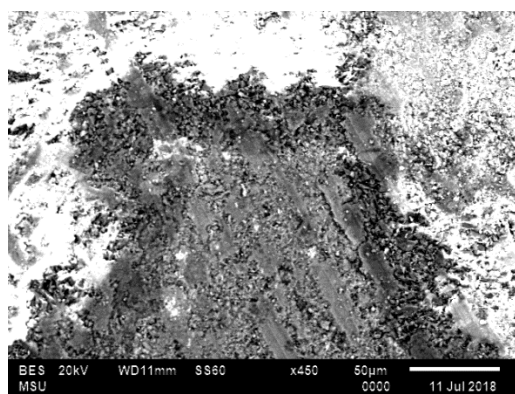


**Figure 3.22.** BS image of zone 3 of the region encircled in dashed blue in Fig.3.21; the image shows parallel bars across the surface.

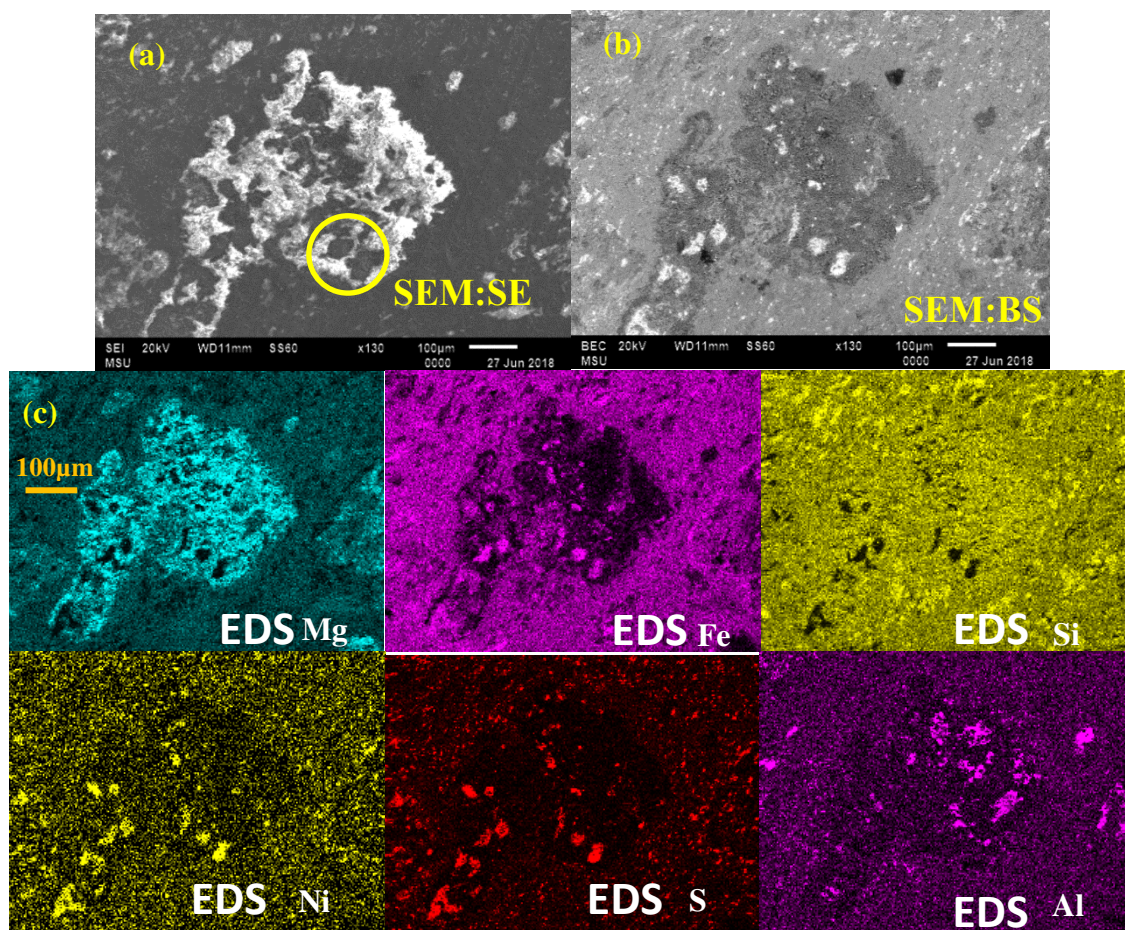


**Figure 3.23** SEM images and EDS maps of zone 4: (a) SE image, (b) BSE image, both at 130X; (c) EDS maps of elements.

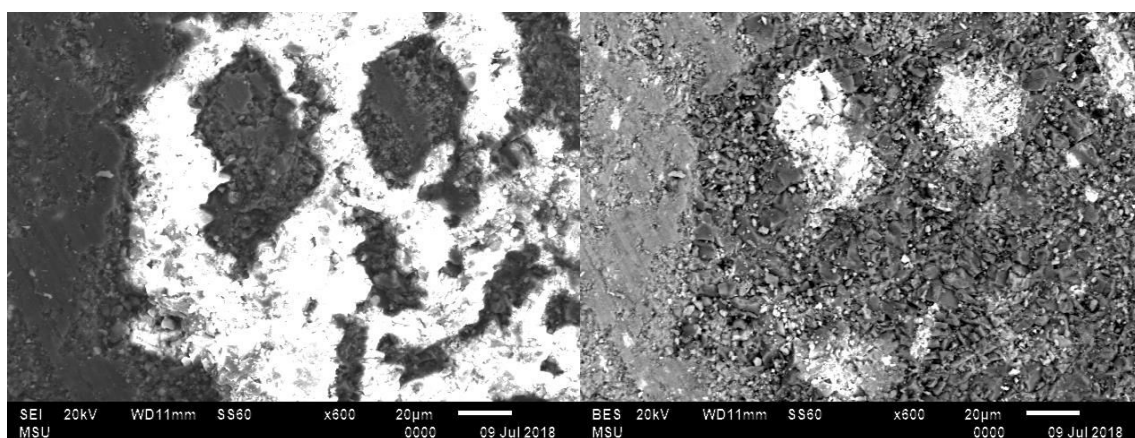


**Figure 3.24.** BS images of the circled region of zone 4 (Fig. 3.23); these two circular areas contained S, Ni and Fe.

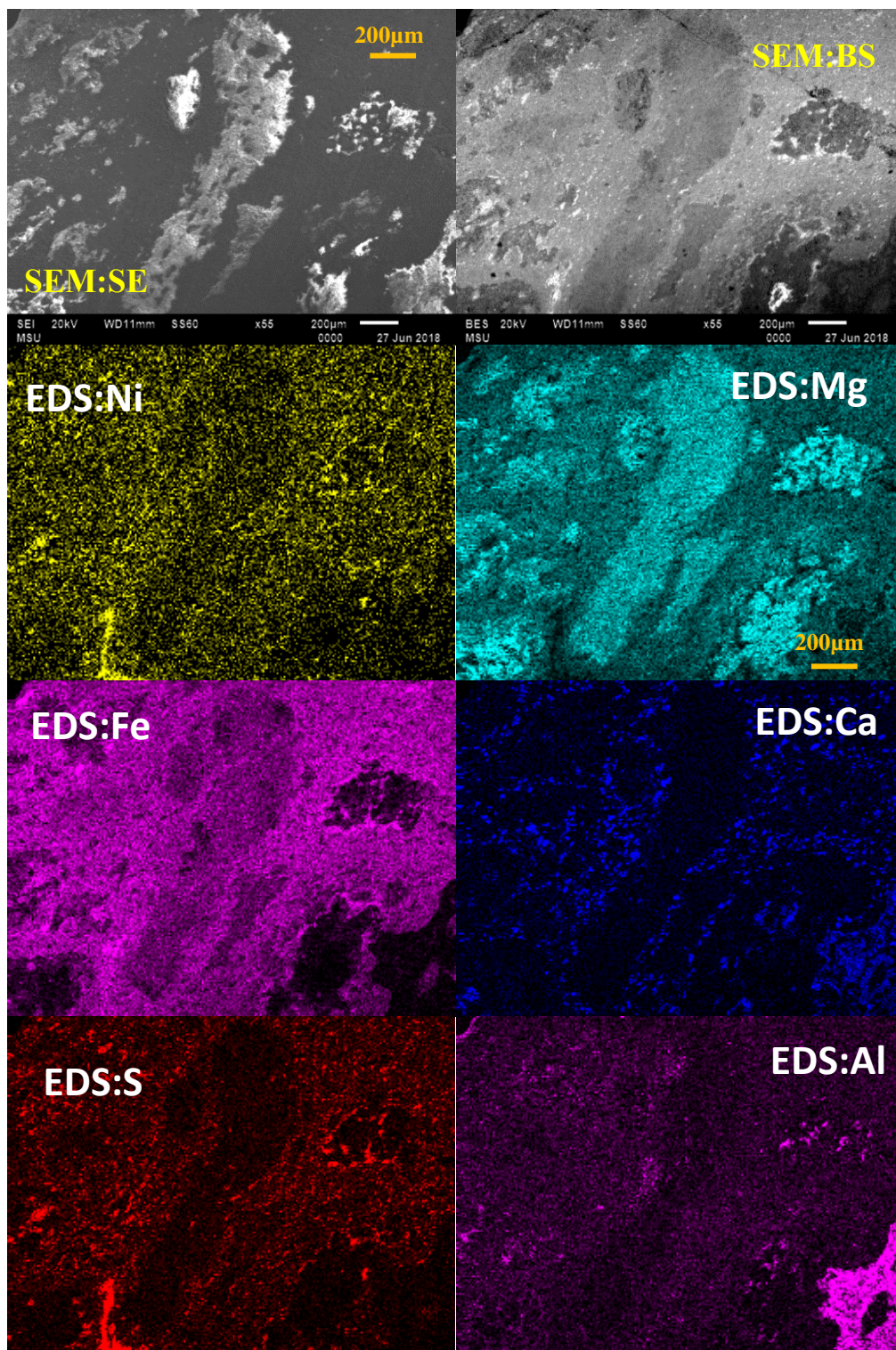
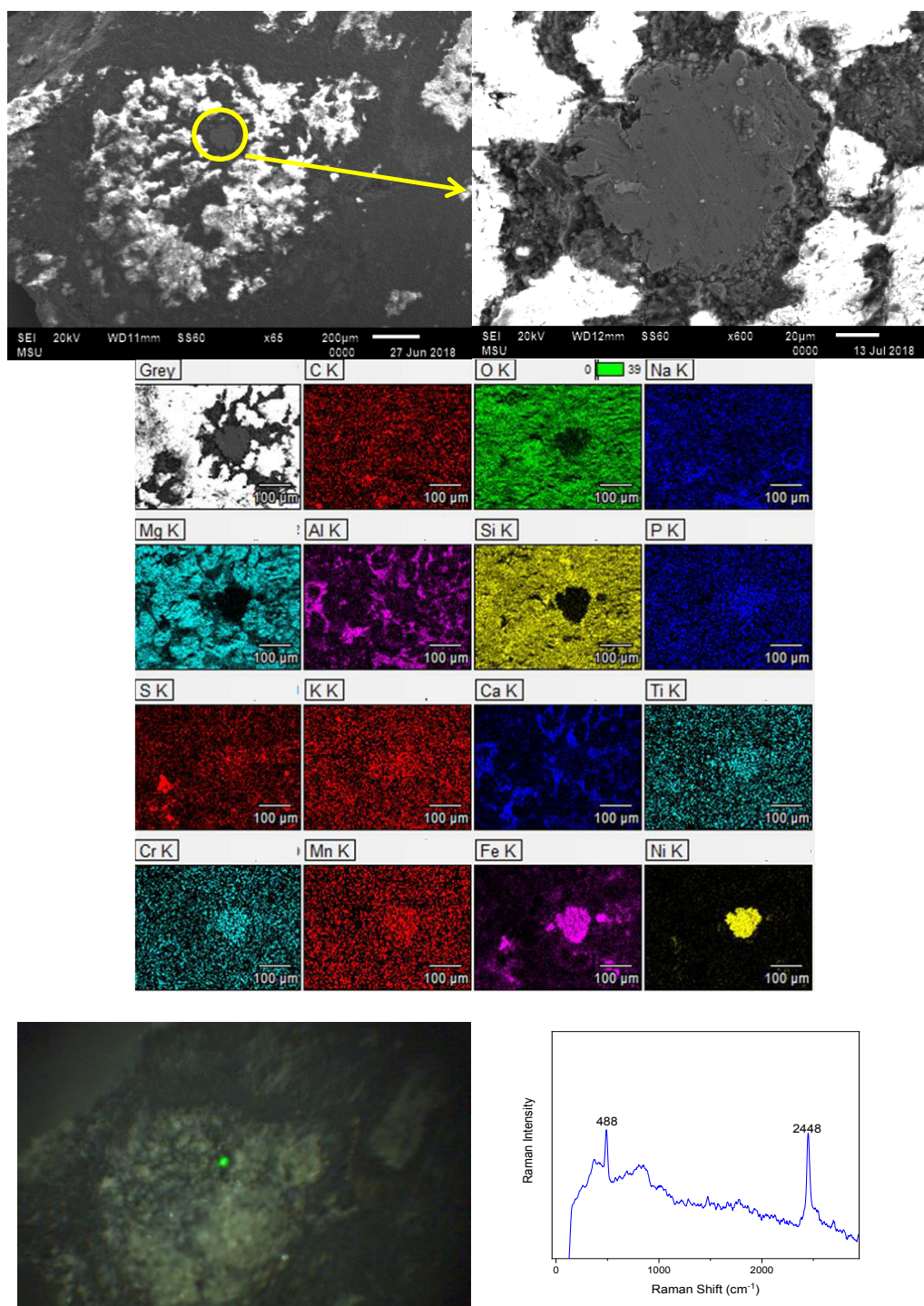


Figure 3.25. SE image, BS image and EDS of zone 2



**Figure 3.26.** SE images and EDS maps (zone 1) corresponding to one of the spots wherefrom the Raman spectrum of an unknown mineral in Bali was obtained; the laser spot is directly upon the Fe-Ni rich region of zone 1.

## 4. Discussion

### 4.1 Features and trends within each chondritic sample

In the Allende meteoritic sample, a total of 10 inclusions were studied. A number of chondrules could be identified within these inclusions by simple inspection. They were white, round; had well-defined boundaries from the matrix, features that are typical to chondrules. The distinct chondrule boundaries are indicative of a less-shocked parent body, i.e. it did not experience much alteration due to high-velocity impacts. Changes due to these impacts cause structural and sometimes chemical alterations in the planetesimals (parent bodies); these changes are quantified by a parameter called 'shock stage'. The shock stages range from S1 (unshocked) to S6 (very strongly shocked). The visual characteristics accompanying each shock stage is usually the olivine crystal structures along with the chondrule shapes. In the literature, Allende has been assigned a shock stage of S1 (Stoffler, 1991) which is indicative of a relatively unshocked parent body, with the maximum pressure generated from the impacts being  $< 5$  GPa.

The optical, Raman and SEM/EDS analysis confirmed that inclusions 1, 4, 5, 6 and 7 have typical characteristics of chondrules. The sizes of these chondrules were approximately 1 mm in diameter. One of the inclusions studied (inclusion 9, Fig. 3.15a), seems to match the descriptions of a porphyritic chondrule: large crystals set in a finer-grained or glassy background (McSween and Huss, 2010). This inclusion covered a wide area and when viewed under the Raman probe camera as well as from its SEM

micrographs, it appears to contain several crystal-like structures. The Raman data taken from some of these structures showed either olivine or pyroxene or a combination of both, and occasionally quartz was also found in them. Inclusions 3 and 2 (Fig. 3.16 and 3.11 respectively) were refractory inclusions: inclusion 3 was most likely an AOA based on its fluffy and irregular structure, further confirmed by olivine spectra from within the inclusion. Inclusion 2 was observed to be spherical, compact with a nearly round circumference; it contained Ca and Al and could therefore be a CAI. The hole-like structures within the inclusions could be indicative of localized evaporation of minerals from those regions. The evaporations could have happened either during the gas condensing from nebula or on the parent body due to secondary heating events.

Some of the chondrules were surrounded by rims and a few were observed to have lined structures stacked parallel to each other (Fig. 3.15b). Raman spectroscopy data obtained from spots on these lined structures gave olivine, which is consistent with other studies (Noguchi, 2002). In general all the chondrules that were studied seemed to be Type I, i.e. those containing poor FeO, and more of MgO-rich silicates. The elemental compositions within the inclusions were fairly consistent with each other, and the mean values of percentage composition by weight are close to those reported in the literature (Hutchinson, 2004).

The carbon content was found to be mostly semi-graphitic (a stage halfway between graphitic carbon and amorphous carbon) in nature (Section 4.3). Olivine and pyroxene were abundant throughout the sample, but in general the inclusions showed a relative excess of pyroxene than the matrix, while the matrix contained a higher relative

amount of olivine than the inclusions. The correlation between presence of Fe and absence of Mg from a given region was also consistent throughout the sample (Section 4.2).

The meteorite fragment from Bali, gave diverse results in its elemental composition as well as in its Raman spectra. The SEM images also show the various differences in the shape and morphology of the inclusions studied. They had varying lengths between less than 1 mm up to 4 mm maximum. None of the inclusions seemed to match the circular and “globule”-like structure of a typical chondrule and it was unclear to locate the boundaries between the inclusions and matrix. This indistinguishable feature where inclusions (potentially chondrules) appear to be merged to one another is typical of a parent body that experienced a certain level of shock metamorphism owing to impacts (Sears, 2004). Bali has been assigned a shock stage of S3 which suggests it to be coming from a weakly shocked parent body (maximum pressure ~15 GPa) (Stoffler, 1991).

In this sample, inclusions 1 and 4 could be porphyritic chondrules. The other inclusions are irregularly shaped and seem to have several smaller clusters around them. These inclusions could either be AOAs or CAIs. The inclusion 2 did not contain any Ca and did contain olivine; also the shape was fluffy and irregular and is thus most likely an AOA. On the other hand, inclusion 3 was entirely filled with Ca and Al and is therefore much likely to be a CAI. However, radiometric measurements would be the appropriate technique to confirm the exact inclusion type. Several parallel barred structures were seen in inclusion 3 (Fig. 3.22). Other structures observed under the Raman probe camera included a golden-brown patch which was crystalline and lustrous in appearance, olivine

crystals (yellow-green) and one shiny glass-like speck all embedded within the matrix. The glass speck is of particular significance since it could be a structure often described in the literature as “GEM”: glass with embedded metal and sulfide. GEMs are minute inclusions consisting of amorphous silicate material bearing bits of iron-nickel and/or iron-sulfide. This spot like some others was also the source of one of the unknown Raman spectra observed in Bali with peaks at 488 and 2448  $\text{cm}^{-1}$ , and Fe-Ni presence was seen in the EDS maps. Thus, it is a possibility that the unknown mineral found in multiple sites of the meteorite was GEM since the peak positions in the Raman spectrum belong in the region typical of silica bearing mineral (Neuville *et al.*, 2014). Unfortunately, its precise elemental composition could not be confirmed from the literature. GEMs are considered to be interstellar in origin i.e., foreign to the solar nebula (McSween, 1999).

The white smaller inclusions had higher relative concentration of Mg-Si-O and low in Fe, while the matrix had relatively more Fe and graphitic C. This sample contained several patches where Fe-Ni would cluster, sometimes also with S or P. These clusters were located either within the inclusion or just outside the boundary separating the inclusion and matrix. Their shapes were either geometrically symmetrical or circular which could imply an underlying well-organized, crystalline structure of the elements. Ca was also observed to cluster in certain regions sometimes with other elements like Al or Na. Similar to the geometric structures of Fe-Ni, Ca and Si or Ca and Al also formed such structures as seen from their EDS maps (Fig. 4.1).

## 4.2 Features and trends between the two chondrite samples

Both chondritic samples had several similar features, such as high concentrations of O, Mg, Fe and Si, and volatile elements such as Cr, Mn and P present only in trace amounts, as is characteristic of CV chondrites. Fe/Mg complementarity was observed in both. Mg dominated the interior of the white inclusions, while Fe was more within the matrix of both samples. The olivine in both was Mg rich ( $F_O > F_a$ ) and the “amorphization” of their C (Section 4.3) also was of a similar extent. All the elemental composition values (wt. %) are close to or in good agreement with the literature (Hutchinson, 2004). Another similarity for both samples was that C was found to accumulate near the edges of the sample, which was confirmed by Raman spectroscopy to be semi-graphitic in nature (Murae et al., 1993). High resolution imaging of other regions where C had clusters revealed planar, smooth and sheet-like structures. However, Raman spectroscopy and SEM images of these planar C sites do not show any known allotropic form such as nanowires, nanotubes or nanodiamonds. Ca and Al showed two trends in both sample: they were either present together in patches, or were complementary to each other. Rims of S were also observed in both samples.

Some distinctions between the two were present as well: while several inclusions in Allende were readily identified as chondrules, Bali presented a much more complex mix in the type of its inclusions. This was attributed to the differences in their shock stages (McSween, 1999), which was also manifested as smaller olivine crystals in the Bali sample with respect to the olivine crystals in the Allende sample (Stoffler, 1991). Several metallic-melts of Fe-Ni round in shape were observed in Bali, whereas no such

structure combination was seen in Allende. Pyroxene (enstatite and diopside) was observed in several spots of Allende, while it was scarcely present in Bali.

The fact that the chondrules and matrix would show such distinct patterns implies that they are chemically related (Hezel and Palme, 2015). Understanding the chemistry connecting these two is vital as it can lead to important implications about their processes. Many theories surround these observations, with various degrees of success in their ability to explain it fully and be compatible with other observations as well. Some of the explanations behind these observations (both similarities and differences) are discussed below:

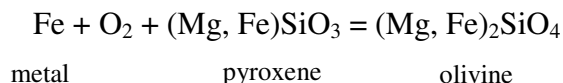
- (i) The chemical complementarity in chondrule and matrix (as seen here in both samples between Fe and Mg; higher Fe in matrix relative to inclusion and the converse for Mg) has been observed widely in carbonaceous chondrites, between Fe/Si (Wood, 1985), Fe/Cr (Klerner, 2001) and several other pairs of minerals. Thus, the complementary relationship has been the subject of many studies (Klerner and Palme, 1999a, Hezel and Palme, 2010; Palme *et al.*, 2015, etc.). A variety of explanations has been proposed to explain this observation; but a consensus has not been arrived at yet. Grossman and Wasson, (1985) suggested that the observed complementarity characteristic was probably due to ejection of liquid (Fe) metal droplets from rotating chondrules. Hezel and Palme (2010) explained that the Mg/Si complementarity (higher Mg in chondrule than in matrix; higher Si in matrix than chondrule) by suggesting that Si evaporated from the chondrule (as

SiO<sub>2</sub> gas) and later condensed in the matrix. Alternatively, the author suggested that perhaps Mg and Si fractionated in different precursor materials, wherein the chondrule precursor was Mg-rich and the matrix precursor had overabundance of Fe. Similar processes could be responsible for the Fe/Mg complementarity observed here in the samples studied. The fact that this complementarity feature has been a prominent observation in many meteorites could mean that the underlying processes have important implications about chondrite formation theories. In their paper, Hezel and Palme (2015) argue that this complementary behavior requires the formation of chondrules and accretion of complementary matrix from a single reservoir (localized nebular region), contrary to several models suggesting independent sources of matrix and chondrules that are located in different areas of the solar nebula.

- (ii) Sulfur rim around inclusions was also observed in both samples, in the form of metal-sulfide rims. In his book, *The Origin of Chondrules and Chondrites*, (2004), Sears (and references therein) talks about the chondrule rims observed in various chondrites and gives several possible formation mechanisms. Podolak *et al.*, (1993) suggested that opaque rims could have formed around chondrules, when the chondrules entered the atmosphere of their parent body. Another possibility is that S-rich vapors condensed onto the boundaries of chondrules in the form of a fine-grained mixture of

sulfides, metals and silicate. Hewins (1991) argued that the rims were formed when nebular dust accreted onto freely floating chondrules. While it is not possible to narrow down the origin of rims to a single explanation, it is however clear that the rims hold much potential in understanding the accretion history of chondrites.

- (iii) Fe-Ni spots (in Bali) were in close proximity (or within) the inclusions. Palme *et al.*, (2015) state in their paper the tendency of Ni to be found co-existing with Fe is owing to its siderophilic (Fe-loving) nature, therefore the existence of Ni-Fe patches within the inclusions could be attributed to the same mechanism as stated in their paper: a liquid metal melt ejecting Fe from the chondrules is picked up by Ni to form metallic Fe-Ni or alloy structures. This mechanism also limits the possibility of matrix being Fe-rich due to Fe-ejection from the chondrules.
  
- (iv) Olivine-pyroxene mixtures (in Allende) were in general Fe-deficient. In fact, both olivine and pyroxene crystals were also Fe-deficient, which could indicate that both minerals were formed in a Fe-deficient environment. The oxidation reaction shown here demonstrates how olivine could disintegrate to give pyroxene; or how pyroxene is oxidized into olivine. Which way the reaction will proceed depends upon the starting materials and physical conditions present (McSween and Huss, 2010).



Based on the works of Larry Grossman (University of Chicago), McSween, (1999) presented a schematic of the condensation sequence that may have occurred. In a diagram (not shown here) he illustrates a chain of steps leading to the formation of one mineral from another given a certain pressure and temperature. It shows that forsterite under high pressure, cools down to generate enstatite; this reaction is also corroborated by the Bowen's reaction series (Fig. 4.3). Therefore, if the olivine has low Fe content to start with, the pyroxene will have lower Fe content as well. In this study, the Raman peaks corresponding to pyroxene were either attributed to a combination of pyroxenes when no olivine was present at that spot. Or, it was observed that the pyroxene peaks were present together with olivine peaks, both shown to be present at the same spot being sampled. When present together (as seen from Raman spectra), the relatively high peaks of pyroxene would be accompanied with lower intensity peaks of olivine, and vice-versa. Hezel and Palme, (2010 and references therein), explain that this is due to an Mg-rich phase serving as the main precursor component for chondrules. Forsteritic olivine is the first major phase to condense out from this melt under a wide range of

nebular conditions (Palme and Fegley, 1990). Pyroxenes form at lower temperatures by reaction of  $\text{SiO}_{(g)}$  (where g stands for gaseous) with forsterite. If cooling of the nebula is sufficiently fast there is not enough time to convert the appropriate amount of forsterite into enstatite (Petaev and Wood, 1998). The result is an Mg-rich phase composed of a mixture of olivine and pyroxene.

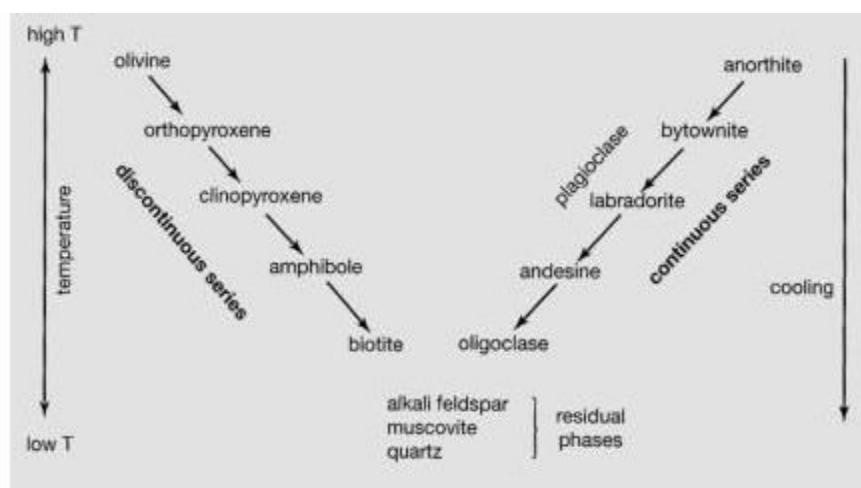


**Figure 4.3.** Schematic illustration of Bowen's reaction series.

### 4.3 Justifications toward a single local parent reservoir

In their work Hezel and Palme, (2010) argue that the Mg/Si complementarity is due to the extraction of an Mg-rich component from the chondritic reservoir, leaving behind an Mg-depleted phase which became the precursor to matrix. This can also be extended to Fe/Mg complementarity as observed here and also in other works (Palme et al., 2015 etc.). It has been already established that the refractory elements (Ca-Al bearing compounds) segregated first within the chondritic reservoir. With lowering of

temperature these initial Ca-Al rich phases convert to other minerals and more elements are removed from the gas as it cools down (Lodders, 2003). Mg condenses as melilite and spinel and more of it is removed when forsterite and enstatite condenses out from the gas (Lodders, 2003, McSween 1999). Metallic Fe has condensation temperatures close to forsterite (Lodders, 2003, McSween 1999), but separates from the chondrule precursor phase in the following manner: first, some of it condenses from the gas phase into metal which is stable and cools down to get incorporated into the chondrites later (McSween, 1999). Between the gas phase of Mg and Fe, Mg is more reactive and hence more of Mg is combined with the Si and forms Mg-rich olivine and pyroxene at temperatures  $\sim 1100^{\circ}\text{C}$ . Since chondrules were formed at higher temperatures ( $>400^{\circ}\text{C}$ ) than the matrix (McSween, 1999) it can thus be extrapolated that these initial Mg-bearing olivine and pyroxene that directly condensed from the gas as liquid droplets were the major bulk of chondrules as has been observed. This leaves behind an excess of Fe in the form of Fe (g) and the metallic Fe which is stable and much less reactive. The less competitive Fe (g) combines with some of the Mg-rich olivine and pyroxene at lower temperatures giving rise to olivine/pyroxene with higher Fe-content (McSween, 1999). Additionally, siderophilic elements like Ni and S react with the metallic Fe to form troilite (FeS) and Fe-Ni alloys at temperatures  $<400^{\circ}\text{C}$  thus forming the bulk of the matrix. Also, S being volatile was present in the gaseous form in the reservoir (Lodders, 2003) and condenses around the chondrules observed as rims. With further lowering of the temperature and localized compaction of these condensed phases of the inclusion, chondrules and matrix gradually form the protoplanets.

Furthermore, a major argument against a chondrite formation model involving separate independent sources of matrix and chondrules that later mix together forming the chondrule is that such models place no constraint on the relative amounts of matrix and chondrule being mixed. Previous measurements quantifying the Fe/Mg ratio in matrix and chondrule show that the values of the ratio among different clans of carbonaceous chondrites are similar to each other. This should not be the case if the chondrules and matrix were indeed formed in separate zones and later mixed together, since in this scenario higher Fe/Mg ratio would be expected in some regions of the accreted body than in others (Palme *et al.*, 2015 and references therein).

#### **4.4 Carbon peak parameters and secondary alterations of the parent body**

After their formation, the chondrules and matrix eventually accreted into planetesimals. These planetesimals were the sources and hosts of the meteorites and were therefore known as their parent bodies. The parent bodies themselves were subjected to several alteration processes (thermal, radioactive, shock, etc.) which affected the composition and structure of its constituents (Huss *et al.*, 2006; Weisberg *et al.*, 2006). The nature of the graphitic carbon present in carbonaceous meteorites is an excellent indicator of some the secondary processes and the extent to which they were experienced by the meteorite parent bodies. In particular, the D- and G- bands present in the Raman spectra of carbonaceous meteorites have been thoroughly analyzed to find correlations between the peak parameters and metamorphoses of the parent body.

The thermal alterations of the parent bodies resulted in acquiring a peak called ‘Peak Metamorphic Temperature’ (PMT). The value (or the range of values) of this temperature can be estimated from the peak parameters of D- and G- bands of graphitic carbon. The process of doing this is called Raman spectroscopic thermometry. By studying the data obtained from several chondrites, a number of ‘thermometers’ (equations relating the spectral parameters to the PMT) have been proposed in the literature (Homma *et al.*, 2015; Bonal *et al.*, 2016; Busemann *et al.*, 2007 etc.). In this study, the works of Homma and Busemann have been applied to the spectra of both samples that showed D- and G-bands.

The D-G bands were fitted using the Lorentzian function in OriginPro. The fitting gives several parameters like the peak position ( $\omega$ ) in  $\text{cm}^{-1}$ , full-width at half-maximum (FWHM,  $\Gamma$ ) in  $\text{cm}^{-1}$  and the peak area integral which corresponds to the peak intensity ( $I$ ).

The Busemann model (Busemann *et al.*, 2007) gives an equation relating the  $\Gamma_D$  to the PMT of the parent body:

$$\text{PMT } (^\circ\text{C}) = (931) - 5.10 \times (\Gamma_D) + 0.0091 (\Gamma_D)^2 \quad (4.1)$$

Using the average value of  $\Gamma_D$  obtained for each sample, their PMTs were calculated to be:

- $(638 \pm 23)^\circ\text{C}$ , for the Allende meteoritic sample; and
- $(583 \pm 15)^\circ\text{C}$ , for the Bali meteoritic sample.

From the Homma model, the PMT is given by:

$$\text{PMT } (^{\circ}\text{C}) = -6.9 \times I_{\text{D}} + 1054.4 \quad (4.2)$$

Applying this, to the spectral data from the samples, gave the following values:

- $(604 \pm 13)^{\circ}\text{C}$ , for the Allende meteoritic sample; and
- $(504 \pm 18)^{\circ}\text{C}$ , for the Bali sample.

In the literature, the PMT for Allende is reported to be between  $(550\sim 600)^{\circ}\text{C}$  by Huss *et al.* (2006),  $590^{\circ}\text{C}$  by Busemann *et al.* (2007) and  $(604 \pm 10)^{\circ}\text{C}$  by Homma *et al.* (2015). Therefore, the values of PMT obtained in this study for Allende using the aforementioned models, are in good agreement with the literature. The PMT values obtained for Bali are fairly close to each other; however it could not be compared to any previous studies since to the best of this research group's knowledge no PMT for Bali were reported in the literature.

In addition to estimating the PMT, the D-G bands also hold clues to know the “nature” of the carbon present in the meteorites, and thus understanding the series of secondary alterations of the parent body. Tuinstra and Koenig (1970) developed a relationship between the graphite peak parameters and the “amount of crystal boundary” of the graphitic sample. Their work was done on artificial carbon samples. However, it was later expanded upon by others and applied to meteorites and other kinds of graphitic samples (De Angelis, *et al.* 2011; Cançado *et al.*, 2006; etc.). It was confirmed by Tuinstra and Koenig (1970) that the “amount of crystal boundary” is related to the average crystal diameter,  $L_a$  (known as the TK relation), which is determined by X-ray techniques. Later works refer to it as simply the “crystallite size” and denote it by  $L_a$ .

Ferrari and Robertson (1999) developed a three-stage model that illustrates the “amorphization” trajectory of graphitic carbon (graphite → nanocrystalline (NC) graphite → amorphous C → totally amorphous (ta) C), and extends the validity of the TK relation beyond its initial applicability range. They used the G-peak position ( $\omega_G$ ) and the ( $I_D/I_G$ ) ratio, showing that the change from graphitic to amorphous is marked by a progressive change in these parameters. The average values of  $\omega_G$  and  $I_D/I_G$  obtained from the samples used in this study were compared to this amorphization scheme. For both samples, the average values ( $\omega_G$  and  $I_D/I_G$ ) belonged to stage 1, which is intermediate between NC-graphite and graphite.

Murae *et al.* (1993) employed the TK relation and chemical (wet) analyses to determine the crystallinity of the graphitic carbon present in carbonaceous chondrites. Combining their results, they showed the threshold values of  $L_a$  required by the various graphitic stages.

$L_a \sim 10 \text{ nm} \rightarrow$ semi-graphitic	 More amorphous
$L_a \sim 20 \text{ nm} \rightarrow$ graphitic	
$L_a \sim \infty \rightarrow$ well-graphitic carbon.	

The TK relation is given as:

$$L_a \text{ (nm)} = 4.5 (I_D/I_G) \text{ for an excitation wavelength } \lambda_l = 515.5 \text{ nm}$$

Cançado *et al.* (2006) developed a general equation for determining  $L_a$  for any laser wavelength (energy):

$$L_a \text{ (nm)} = (2.4 \times 10^{-10}) \lambda_l (I_D/I_G)^{-1}$$

Applying the above equation to this research, where the laser wavelength had a value 532 nm, the average  $L_a$  (nm) was found to be:

- 13.64 nm, for Allende
- 14.85 nm, for Bali

This implies the graphitic carbon of both samples to lie between “semi-graphitic” and “graphitic”, as per the Murae classification. This agrees well with the results obtained from the Ferrari and Robertson’s amorphization trajectory, which also indicated nanocrystalline graphite to be present in these samples. It is noteworthy that the  $L_a$  values were obtained using the average values of  $I_D$  and  $I_G$ ; however the ( $I_D/I_G$ ) ratio varied from 2.4 to 0.8 for Allende and from 2.0 to 0.6 for Bali. This suggests that the graphitization of the sample was heterogeneous; sometimes even along a single vein, wherein two dissimilar values for ( $I_D/I_G$ ) ratio can be obtained by sampling adjacent spots. This heterogeneity along a single vein could be a result of two stage crystal growth of graphite in the vein: 1) crystallization of graphite from molten metallic phase, and 2) by injection of less-ordered C into the vein from the static part of the parent body (Murae *et al.*, 1993). The  $\Gamma_D$  values along with the  $I_D/I_G$  ratio is a good indicator of the maturation grade (Beyssac *et al.*, 2003; Chaumard *et al.* 2013, etc.) of the carbon content, i.e. it indicates the graphitic extent of the sample. The organic matter in the sample undergoes carbonization followed by graphitization along the maturation process, using the plot from the works of Chaumard *et al.* (2013) (Fig. 4.4), the Bali sample is seen to have been relatively less matured, as its values ( $\Gamma_D$  and  $I_D/I_G$ ) lie on the carbonization curve as

compared to the Allende sample (also presented in their work) whose values indicate higher degree of maturation and hence alteration.

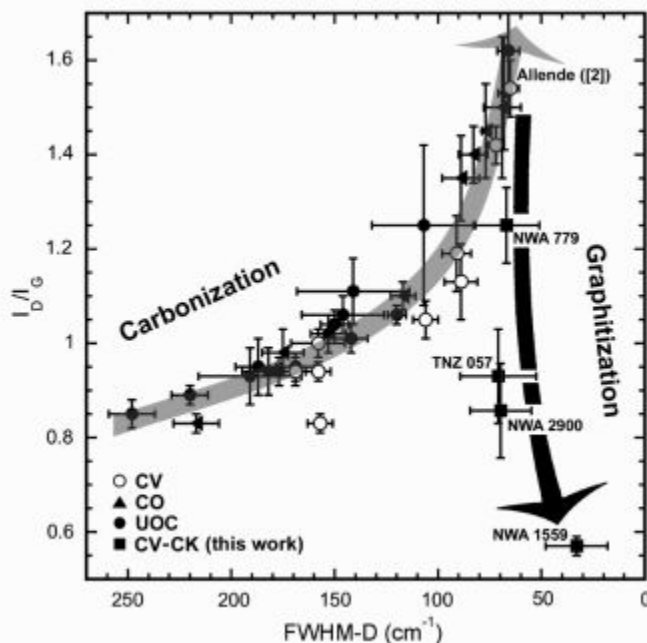


**Figure 4.3.** Diagram showing the plot referred to analyze the samples used in this study. It demonstrates the metamorphic progress of the sample based on its carbon content (Chaumard *et al.*, 2013).

It is known from the literature that the Allende parent body was more heavily metamorphosed than that of Bali (Bonal *et al.*, 2006, 2016). In their work, Bonal *et al.* (2006) conclude that Allende experienced higher thermal maturity than Bali as well, and its petrologic type (PT) was updated from 3.2 to be >3.6; whereas Bali being relatively less thermally altered has a PT of ~3.6. The peak parameters used as maturity tracers by the authors (Bonal *et al.*, 2016) have been compared to the samples in this study, and the results agree well with those stated in the literature.

## 5. Conclusion

In this work, two chondritic meteorite samples were analyzed: Allende and Bali. Both are carbonaceous chondrites and belong to the CV3 class. Micro-Raman spectroscopy was used to analyze the mineral content in each sample, and the compositional and morphological studies were done using SEM/EDS.

For the Allende sample, 10 zones were chosen for this study. Each zone either had a combination of matrix-inclusion or was entirely an inclusion. The inclusions in zones 1, 4, 5, 6 and 7 were identified to be chondrules, and inclusion 9 and 2 were porphyritic chondrules. The inclusions in zones 2 and 4 had S-rims around them. The Fe/Mg complementarity characteristic in the inclusion-matrix composition was fairly homogeneous throughout the sample, with the inclusions having higher relative Mg than the matrix, while the matrix was relatively rich in Fe. Several clusters of Ca and Al were present both within the matrix and inclusions; however, the elements were also seen elsewhere in the zones with no correlation to each other. O was present throughout the zones and C was present sparsely, sometimes concentrated over a small region. These C-rich regions under BSE imaging appeared to be flat, sheet-like in structure. Some trace elements such as Mn, Cr and P were also identified by EDS.

Minerals such as olivine, pyroxene and quartz were seen from the Raman spectra of the sample. Few olivine crystals were visible and identified to be 100% forsterite in composition, while other olivine spectra showed mixed amount of fayalite-forsterite from the spots sampled. Pyroxene was present always as a combination of enstatite-diopside or

enstatite-ferrosilite. The matrix was rich in graphitic carbon, with a varying degree of amorphization. The peak parameter analysis of the carbon D- and G- bands gave an average crystallite diameter of 13.64 nm which implies a semi-graphitic lattice. The D- and G- peak parameters were also used to calculate the PMT of the parent body obtaining an average value of  $\sim 621$  °C.

For the Bali sample, 4 zones were studied. The inclusions in zone 1 and 4 were porphyritic chondrules. The inclusions in the other zones were irregularly shaped unlike typical chondrules and the non-uniformity of their shapes could be due to shock impacts experienced by the parent body, resulting in deformity of chondrule structures. This was in contrast to the Allende sample, with its perfectly round chondrules indicative of an unshocked parent body. Bali also showed the presence of S-rims, Fe/Mg complementarity features and Ca-Al clusters. Several Fe-Ni and Fe-Ni-S spots were seen in Bali. In particular, the Fe-Ni spots were geometrically symmetrical and visible with the naked eye. In the case of Allende, the Ni content was relatively much lower (measured as Ni per unit area sampled). Minerals identified using Raman spectroscopy were olivine, awaruite, larnite and olivine. Graphitic carbon was also present. From the analysis of its spectrum bands, the average PMT was of  $\sim 544$  °C. The average crystallite size was 14.85 nm.

The thermal metamorphism of the Bali parent body was less than that undergone by the Allende parent body. The carbon content in Bali was also found to be less matured

than the Allende. However, the structural alterations due to impacts were higher in Bali than they were in Allende.

In general, two observations were of particular interest: 1) the formation of S-rims around inclusions, and 2) the complementarity characteristic of Fe/Mg. The S-rims indicate the possibility of chondrules as free floating globules before getting compacted into parent bodies. The Fe/Mg complementarity feature can be satisfactorily explained by a model where the chondrule and matrix formation has taken place in the same local nebular region. This picture of a same parent reservoir can also successfully explain the chemistry behind the Fe-Ni alloy spots and the S-rims by taking into account the volatility and chemical reactivity of the elements.

More research is required to fully validate any model to describe the planet formation mechanism in detail. Several analyses have been done in this study and findings about the parent bodies of the meteorites have been presented (in particular for Bali, which has been scarcely studied). By studying the elemental and mineralogical composition of the samples and deciphering the trends within, implications about the chondritic component formation have been provided. Thus, the presented findings can contribute to unravel the mysteries surrounding the creation of these relics.

## Acknowledgements

The conception, progress and ultimate completion of this work has been possible due to inputs from a lot of different people. First and foremost, I am extremely grateful to my advisor, Dr. Analía "Yanil" Dall'Asén, whose expertise, knowledge, wisdom, guidance and patience has been monumental in helping me achieve this landmark. The time and effort she put toward making my Masters' program successful is immeasurable, as was her willingness to help at every step. Undoubtedly, while training under her I have been able to grasp and better appreciate the various skills of an experimentalist.

I am also thankful to Dr. Steven Losh and Dr. Andrew Roberts for their consent to be part of my thesis defense committee; Dr. Losh's feedback and suggestions have been of much help. Sincere thanks to Dr. Mike Bentley for allowing us research time on the SEM/EDS equipment. Physics Technician and Engineering Aide Senior of MSU Mr. Mike Peters has been a key part of this research with his contribution as a technical support specialist at several stages. The help and initial equipment training by fellow graduate student Aaron Stokke is highly appreciated. Rohil Kayastha, another undergraduate member of this research group, also contributed greatly by cataloguing all the meteoritic samples.

I am indebted to every faculty member of The Department of Physics and Astronomy for supporting me infinitely at a time of crisis I encountered during my time here, without which none of this would be achievable. Special thanks to Dr. Dall'Asén,

Dr. Roberts and Dr. Brown for devoting their personal time in helping me overcome the same crisis.

Other people whose contribution and assistance made a great difference are Elizabeth (Betsy) Olson, Marcus Franczak, Cindy Flitter, Jodi Egeland, Rohil Kayastha and Dr. Youwen Xu. Their aid, assurances and presence during more than one critical junction have played a big role in the finality of this thesis.

Lastly, I would like to express my gratitude to my family and friends overseas, for strengthening the foundations of my ambition always; especially to my parents for their continued support, love and enthusiasm and my grandparents for instilling the curiosity of a scientist in me.

## References

- Beyssac, O., Goffé, B., Chopin, C., & Rouzaud, J. N. (2002). Raman spectra of carbonaceous material in metasediments: a new geothermometer: RAMAN SPECTROSCOPY OF CARBONACEOUS MATERIAL. *Journal of Metamorphic Geology*, 20(9), 859–871. <https://doi.org/10.1046/j.1525-1314.2002.00408.x>
- Bonal, L., Quirico, E., Bourot-Denise, M., & Montagnac, G. (2006). Determination of the petrologic type of CV3 chondrites by Raman spectroscopy of included organic matter. *Geochimica et Cosmochimica Acta*, 70(7), 1849–1863. <https://doi.org/10.1016/j.gca.2005.12.004>
- Bonal, L., Quirico, E., Flandinet, L., & Montagnac, G. (2016). Thermal history of type 3 chondrites from the Antarctic meteorite collection determined by Raman spectroscopy of their polyaromatic carbonaceous matter. *Geochimica et Cosmochimica Acta*, 189, 312–337. <https://doi.org/10.1016/j.gca.2016.06.017>
- Bowen, N.L. (1956). *The Evolution of the Igneous Rocks*. Canada: Dover. pp. 60–62.
- Busemann, H., Alexander, M. O., & Nittler, L. R. (2007). Characterization of insoluble organic matter in primitive meteorites by microRaman spectroscopy. *Meteoritics & Planetary Science*, 42(7–8), 1387–1416. <https://doi.org/10.1111/j.1945-5100.2007.tb00581.x>
- Cançado, L. G., Takai, K., Enoki, T., Endo, M., Kim, Y. A., Mizusaki, H., ... Pimenta, M. A. (n.d.). General equation for the determination of the crystallite size  $L_a$  of nanographite by Raman spectroscopy. *Appl. Phys. Lett.*, 4.

- Chaumard, N., & Devouard, B. (2016). Chondrules in CK carbonaceous chondrites and thermal history of the CV–CK parent body. *Meteoritics & Planetary Science*, *51*(3), 547–573. <https://doi.org/10.1111/maps.12599>
- Dall'Asén, A. G., Dimas, S. I., Tyler, S., Johnston, J. F., Anderton, T. R., Ivans, I. I., Kenyon, S. J. (2017). Mapping the composition of chondritic meteorite Northwest Africa 3118 with micro-Raman spectroscopy. *Spectroscopy Letters*, *50*(8), 417–425. <https://doi.org/10.1080/00387010.2017.1346689>
- De Angelis, S., Corte, V. D., Baratta, G. A., Rietmeijer, F. J. M., Brunetto, R., Palumbo, P., Rotundi, A. (2011). Raman Microspectroscopy Performed on Extraterrestrial Particles. *Spectroscopy Letters*, *44*(7–8), 549–553. <https://doi.org/10.1080/00387010.2011.610424>
- Faria, D. L. A. de, Silva, S. V., & Oliveira, M. T. de. (1997). Raman microspectroscopy of some iron oxides and oxyhydroxides. *Journal of Raman Spectroscopy*, *28*(11), 873–878. [https://doi.org/10.1002/\(SICI\)1097-4555\(199711\)28:11<873::AID-JRS177>3.0.CO;2-B](https://doi.org/10.1002/(SICI)1097-4555(199711)28:11<873::AID-JRS177>3.0.CO;2-B)
- Ferrari, A. C., & Robertson, J. (2000). Interpretation of Raman spectra of disordered and amorphous carbon. *Physical Review B*, *61*(20), 14095–14107. <https://doi.org/10.1103/PhysRevB.61.14095>
- Ferraro, J. R., Nakamoto, K., & Brown, C. W. (2003). *Introductory Raman spectroscopy* (2nd ed). Amsterdam ; Boston: Academic Press.
- Goldstein, J. (2017). *Scanning electron microscopy and x-ray microanalysis* (4th edition). New York, NY: Springer Science+Business Media, LLC.

- Grady, M. M., Hutchison, R., England, N. H. M. (London, & Graham, A. (2000). *Catalogue of Meteorites Reference Book with CD-ROM*. Cambridge University Press.
- Grossman, J. N., & Wasson, J. T. (1985). The origin and history of the metal and sulfide components of chondrules. *Geochimica et Cosmochimica Acta*, 49(4), 925–939. [https://doi.org/10.1016/0016-7037\(85\)90308-4](https://doi.org/10.1016/0016-7037(85)90308-4)
- Grossman, L., & Larimer, J. W. (1974). Early chemical history of the solar system. *Reviews of Geophysics*, 12(1), 71–101. <https://doi.org/10.1029/RG012i001p00071>
- Hafner B. 2015a. Scanning Electron Microscopy Primer.
- Hafner B. 2015b. Energy Dispersive Spectroscopy on the SEM: A Primer
- Hewins, R. H. (1991). Retention of sodium during chondrule melting. *Geochimica et Cosmochimica Acta*, 55(4), 935–942. [https://doi.org/10.1016/0016-7037\(91\)90152-U](https://doi.org/10.1016/0016-7037(91)90152-U)
- Hezel, D. C., & Palme, H. (2010). The chemical relationship between chondrules and matrix and the chondrule matrix complementarity. *Earth and Planetary Science Letters*, 294(1–2), 85–93. <https://doi.org/10.1016/j.epsl.2010.03.008>
- Holt, D. B., & Joy, D. C. (2013). *SEM Microcharacterization of Semiconductors*. Academic Press.
- Homma, Y., Kouketsu, Y., Kagi, H., Mikouchi, T., & Yabuta, H. (2015). Raman spectroscopic thermometry of carbonaceous material in chondrites: four–band fitting analysis and expansion of lower temperature limit. *Journal of Mineralogical and Petrological Sciences*, 110(6), 276–282. <https://doi.org/10.2465/jmps.150713a>

- Huang, E., Chen, C. H., Huang, T., Lin, E. H., & Xu, J. (2000). Raman spectroscopic characteristics of Mg-Fe-Ca pyroxenes. *American Mineralogist*, 85(3–4), 473–479. <https://doi.org/10.2138/am-2000-0408>
- Huss, G. R., Rubin, A. E., & Grossman, J. N. (n.d.). Thermal Metamorphism in Chondrites, 21.
- Hutchison, R. (2004). *Meteorites: a petrologic, chemical and isotopic synthesis*. Cambridge: Cambridge Univ. Press.
- Kayastha R., R. Paul, A.R. Stokke, A.G. Dall'Asén. “Mineralogical and Elemental Composition of Carbonaceous Meteorite Allende by micro-Raman Spectroscopy and SEM/EDS”. *MSU Undergraduate Research Symposium*. Mankato, Minnesota, USA. April 2018.
- Klerner, S., & Palme, H. (1999). Origin of Chondrules and Matrix in the Renazzo Meteorite. *Meteoritics and Planetary Science Supplement*, 34, A64.
- Klerner, Susanne. (n.d.). Tag der mündlichen Prüfung: 16.05.200, 125.
- Krot, A. N., Petaev, M. I., Scott, E. R. D., Choi, B.-G., Zolensky, M. E., & Keil, K. (1998). Progressive alteration in CV3 chondrites: More evidence for asteroidal alteration. *Meteoritics & Planetary Science*, 33(5), 1065–1085. <https://doi.org/10.1111/j.1945-5100.1998.tb01713.x>
- Kuebler, K. E., Jolliff, B. L., Wang, A., & Haskin, L. A. (2006). Extracting olivine (Fo–Fa) compositions from Raman spectral peak positions. *Geochimica et Cosmochimica Acta*, 70(24), 6201–6222. <https://doi.org/10.1016/j.gca.2006.07.035>

- McSween, H. Y. (1999). *Meteorites and their parent planets* (2nd ed). Cambridge ; New York: Cambridge University Press.
- McSween, H. Y., & Huss, G. R. (2010). *Cosmochemistry: probing the origin and chemical evolution of the solar system*. Cambridge: Cambridge Univ. Press.
- Murae T., et al., Primitive Solar Nebula and Origin of Planets, 479-501, 1993
- Neuville, D. R., de Ligny, D., & Henderson, G. S. (2014). Advances in Raman Spectroscopy Applied to Earth and Material Sciences. *Reviews in Mineralogy and Geochemistry*, 78(1), 509–541. <https://doi.org/10.2138/rmg.2013.78.13>
- Noguchi, T. (2002). Estimation of three-dimensional internal structures of some barred olivine chondrules in Allende (CV3) chondrite. *Antarctic Meteorite Research*, 15, 59.
- Norton O. R., and Chitwood L. 2008. *Field Guide to Meteors and Meteorites*, London: Springer-Verlag.
- Palme, H., & Fegley, B. (1990). High-temperature condensation of iron-rich olivine in the solar nebula. *Earth and Planetary Science Letters*, 101(2), 180–195. [https://doi.org/10.1016/0012-821X\(90\)90152-N](https://doi.org/10.1016/0012-821X(90)90152-N)
- Palme, H., Hezel, D. C., & Ebel, D. S. (2015). The origin of chondrules: Constraints from matrix composition and matrix-chondrule complementarity. *Earth and Planetary Science Letters*, 411, 11–19. <https://doi.org/10.1016/j.epsl.2014.11.033>
- Petaev, M. I., & Wood, J. A. (1998). The condensation with partial isolation (CWPI) model of condensation in the solar nebula. *Meteoritics & Planetary Science*, 33(5), 1123–1137. <https://doi.org/10.1111/j.1945-5100.1998.tb01717.x>

- Podolak, M., Bunch, T., Paque, J. M., Reynolds, R., & Prialnik, D. (1993). Meteorite Ablation Rinds as Analogs for the Origin of Rims on Chondrules. *Meteoritics*, 28. Retrieved from <http://adsabs.harvard.edu/abs/1993Metic..28..334B>
- Raman, C. V. (1929). Part II.—The Raman effect. Investigation of molecular structure by light scattering. *Transactions of the Faraday Society*, 25(0), 781–792. <https://doi.org/10.1039/TF9292500781>
- Reed, S. J. B. (2005). *Electron Microprobe Analysis and Scanning Electron Microscopy in Geology*. Cambridge University Press.
- [Sanders, S ] in A new age in scanning electron microscopy: Applications in the life sciences (Science/AAAS, Washington, DC, 2017), p. [2]
- Scott, M. (n.d.). Larnite - RRUFF Database: Raman, X-ray, Infrared, and Chemistry. Retrieved November 12, 2018, from <http://rruff.info/larnite/display=default/>
- Sears, D.W., et al., (1980) Measuring the metamorphic history of unequilibrated ordinary chondrites. *Nature*, 287, 791-795.
- Sears, D. W. G. (2004). *The origin of chondrules and chondrites*. Cambridge, UK ; New York: Cambridge University Press.
- Shigley, J. (n.d.). R070671 - RRUFF Database: Raman, X-ray, Infrared, and Chemistry. Retrieved November 12, 2018, from <http://rruff.info/tags=597/R070671>
- Stöffler, D., Keil, K., & Edward R.D, S. (1991). Shock metamorphism of ordinary chondrites. *Geochimica et Cosmochimica Acta*, 55(12), 3845–3867. [https://doi.org/10.1016/0016-7037\(91\)90078-J](https://doi.org/10.1016/0016-7037(91)90078-J)

- Stokke, A. (2018). Compositional and Topographical Characterization of Carbonaceous Chondritic Meteorites Moss and Murray Using micro-Raman Spectroscopy and SEM/EDS, 74.
- Tribaudino, M., Mantovani, L., Bersani, D., & Lottici, P. P. (2012). Raman spectroscopy of (Ca,Mg)MgSi<sub>2</sub>O<sub>6</sub> clinopyroxenes. *American Mineralogist*, 97(8–9), 1339–1347. <https://doi.org/10.2138/am.2012.4057>
- Tuinstra, F., & Koenig, J. L. (1970). Raman Spectrum of Graphite. *The Journal of Chemical Physics*, 53(3), 1126–1130. <https://doi.org/10.1063/1.1674108>
- Weisberg, M. K., McCoy, T. J., & Krot, A. N. (2006). Systematics and Evaluation of Meteorite Classification, 34.
- Wood, J. A. (1985). Meteoritic constraints on processes in the solar nebula (pp. 687–702). Presented at the Protostars and Planets II. Retrieved from <http://adsabs.harvard.edu/abs/1985prpl.conf..687W>